Non-canonical transamination metabolism of glutamine sustains efferocytosis by coupling oxidative stress buffering to oxidative phosphorylation.

Johanna Merlin[1*], Stoyan Ivanov[1*], Alexey Sergushichev[2], Julie Gall[1], Marion Stunault[1], Marion Ayrault[1], Amanda Swain[3], Francois Orange[4], Alexandre Gallerand[1], Emmanuel L. Gautier[5], Thierry Berton[6], Jean-Charles Martin[6], Stefania Carobbio[7], Justine Masson[8], Inna Gaisler-Salomon[8], Pierre Maechler[7], Stephen Rayport[8], Judith C. Sluimer[9], Erik A. L. Biessen[9], Rodolphe R. Guinamard[1], Edward B. Thorp[10], Maxim N. Artyomov[3] and Laurent Yvan-Charvet[1]

*These authors contributed equally to this work

[1]Institut National de la Santé et de la Recherche Médicale (Inserm) U1065, Université Côte d'Azur, Centre Méditerranéen de Médecine Moléculaire (C3M), Atip-Avenir, Fédération Hospitalo-Universitaire (FHU) Oncoage, 06204 Nice, France (J.M., S.I., J.G., M.S., M.A., A.G., R.G., L.Y.C.)

[2]Computer Technologies Department, ITMO University, Saint Petersburg, Russia (A.S.)

[3]Department of Pathology and Immunology, Washington University School of Medicine, St. Louis, MO, USA (A.S., M.N.A.)

[4]Université Côte d'Azur, Centre Commun de Microscopie Appliquée (CCMA), 06108 Nice, France (F.O)

[5]Sorbonne Université, INSERM, UMR_S 1166 ICAN, F-75013 Paris, France (E.L.G).

[6]Centre de Recherche Cardiovasculaire et Nutritionnelle (C2VN), INSERM, Institut National de la Recherche Agricole (INRA), BioMet, Aix-Marseille University, Marseille, France (T.B., J.C.M.)

[7]Department of Cell Physiology and Metabolism; Faculty Diabetes Centre, University of Geneva Medical Centre, Geneva, Switzerland (S.C., P.M.)

[8]Department of Psychiatry, Columbia University, USA; Department of Molecular Therapeutics, NYS Psychiatric Institute, USA (J.M., I.G.S., S.R)

[9]Department of Pathology, Cardiovascular Research Institute Maastricht, Maastricht University Medical Center, Maastricht, the Netherlands (J.C.S., E.A.L.B.)

[10]Department of Pathology, Northwestern University, Feinberg School of Medicine, Chicago, Illinois 60611, USA (E.B.T.)

Address correspondence to LYC: yvancharvet@unice.fr

Key words: Macrophage, Glutaminolysis, Efferocytosis, Interleukin-4 and Atherosclerosis

Summary

Tissue macrophages rely on tightly integrated metabolic rewiring to maintain tissue integrity and continuously clear dying neighboring cells. We identify a critical role for glutaminase (Gls) 1 in promoting apoptotic cell (AC) clearance by macrophages (efferocytosis) after interleukin-4 (IL-4) stimulation or upon multiple rounds of AC exposure. Mice selectively lacking macrophage glutaminolysis showed defective efferocytosis *in vivo* and significant pathologic consequences in atherosclerotic lesions. A strong correlation between Gls1 expression and plaque necrosis was discovered in human atherosclerotic plaque. Most cells utilize glutamate dehydrogenase (Glud1) to fuel α-ketoglutarate (α–KG) into the tricarboxylic acid (TCA) cycle for anapleurosis and epigenetic modifications. However, high-throughput transcriptional and metabolic profiling revealed that macrophage effector and clearance functions rely on a non-canonical transaminase pathway to meet the demand for high energy cytoskeletal rearrangements and cellular detoxification requirements. Thus, our non-biased systems approach identifies that efficient ACs clearance has a previously unknown reliance on non-canonical glutamine metabolism.

Highlights

• Macrophage Gls1 facilitates apoptotic cell (AC) clearance in the presence of IL-4 or during continued clearance of ACs.

• Macrophage-specific glutaminolysis inhibition led to defective efferocytosis in atherosclerotic lesions.

• Glud1 deficiency does not recapitulate the defective efferocytosis of Gls1 deficient macrophages.

• High-throughput profiling revealed that efferocytosis relied on a non-canonical transamination metabolism of glutamine to support the high energy actin dynamics.

Introduction

Clearance of apoptotic cells (ACs) by macrophage (i.e, efferocytosis) prevent the leakage of cellular contents from dying cells to maintain tissue integrity in normal physiology (Kojima et al., 2017; Elliott and Ravichandran, 2016). Impaired efferocytosis in disease can have multiple causes, but defects in multiple AC internalization, a process termed 'continual efferocytosis', has emerged as a culprit of many chronic inflammatory diseases such as atherosclerosis (Wang et al., 2017; Yurdagul et al., 2020). Resolution and repair processes also require the cytokine interleukin-4 (IL-4) (Bosurgi et al., 2017) and an efficient metabolic reprogramming to sustain continual efferocytosis (Han and Ravichandran, 2011). However, these separate observations have never been linked at the molecular level.

Glutamine metabolism is considered as a 'fuel for the immune system' and is routinely used as a component for clinical supplementation in trauma patients. Glutamine is initially hydrolyzed into glutamate by the glutaminase Gls1 in a metabolic process called glutaminolysis (DeBerardinis and Cheng, 2010; O'Neill and Pearce, 2016). This is the most upregulated pathway in alternatively activated macrophages (Jha et al., 2015) but whether it supports the metabolic reprogramming of efferocytosis beyond glucose and fatty acid metabolism is not known (Morioka et al., 2018; Zhang et al., 2019).

Here, we tested the hypothesis that glutaminolysis plays a critical role in macrophage effector function. Mice lacking macrophage Gls1 exhibited defective efferocytosis *in vivo* and significant pathologic consequences in atherosclerotic lesions of fat-fed ApoE$^{-/-}$ mice. This was recapitulated *in vitro* after IL-4 stimulation or upon multiple rounds of AC exposure, which are two physiologic paradigms. Mechanistically, we found that glutamate is channeled into the malate-aspartate shuttle by aspartate aminotransferase (GOT)-dependent transamination in order to meet the demand for cellular detoxification and high energy cytoskeletal rearrangements.

Results

To investigate broader metabolic roles of macrophage Gls1 during effector and clearance functions, mice bearing a conditional allele for glutaminase 1 ($Gls1^{fl/fl}$) in macrophages were generated by crossing to Lysozyme-Cre transgenic mice (LysM-Cre). LysM-Cre x $Gls1^{fl/fl}$ peritoneal cavity macrophages ($Mac^{\Delta Gls1}$ PCMs) efficiently deleted *Gls1* and lowered cellular glutamate levels by 2-fold compared to control macrophages (**Fig. 1a**). Although *Gls1* was expressed to various levels in PCMs, bone marrow (BM) monocytes/macrophages, red pulp macrophages (RPMs), Kupffer cells and microglia (**Fig. S1a**), macrophage numbers were similar in all these tissues in $Mac^{\Delta Gls1}$ mice (**Fig. S1b**). Consistently, proliferation and apoptosis were similar in $Mac^{\Delta Gls1}$ PCMs compared to control cells (**Fig. S1c**). Levels of phospho-S6 and Myc protein, mTORC1 downstream targets, were also unchanged in these cells (**Fig. S1d**) along with absence of transcriptional regulation of rapamycin (mTOR), hypoxia or ferroptosis targets (**Fig. S1e**). This rules out a role for glutaminolysis in macrophage maintenance or development at steady state (Dixon et al., 2012; Nicklin et al., 2009). Consistent with the proposed role for macrophage glutaminolysis in efficient IL-4 response (Jha et al., 2015), we observed an impaired induction of canonical M2 genes (*Clec10a*, *Tgm2*, *Arg1*, *Stab1*, *Sepp1*) (**Fig. S1f**) and cell surface expression of CD206 and CD301 (**Fig. S1g**) in $Mac^{\Delta Gls1}$ PCMs suggesting defective macrophage effector function. Additionally, challenging PCMs with either IL-4, apoptotic cells (ACs) or IL-4 and ACs together revealed that Gls1-dependent glutaminolysis was significantly required for efficient efferocytosis in alternatively activated macrophages as measured by the 28% phagocytic index reduction of $Mac^{\Delta Gls1}$ PCMs after 45 min exposure to apoptotic thymocytes (**Fig. 1b**). Similar findings were confirmed in bone marrow-derived macrophages (BMDMs) (data not shown). To test the impact of glutaminolysis on efferocytosis during heightened metabolic challenge, we challenged Gls1-deficient macrophages to continued clearance of ACs, which mimics tissue states of high cell turnover (Han and Ravichandran, 2011). We performed a validated two-stage efferocytosis experiment in which BMDMs were first incubated for 45min with unlabeled ACs and, after AC removal and one-hour interval, incubated with a second round of labelled ACs (Wang et al., 2017). Consistent with the hypothesis, the percentage of macrophages that had internalized the second round of ACs was significantly decreased in Gls1-deficient macrophages than in controls (**Fig. 1c**). Overexpression of Gls1 in BMDMs using lentiviral particles enhanced efferocytosis in un-stimulated control cells and rescued the defective efferocytosis observed in alternatively activated $Mac^{\Delta Gls1}$ macrophages (**Fig. S1h**). To test the *in vivo* significance, we intravenously injected fluorescently labeled ACs into controls and $Mac^{\Delta Gls1}$ mice. Gls1 deficiency reduced the ability of $CD11b^{lo}F4/80^{high}$ Kupffer cells (KCs) in the liver and to some extent $CD11b^{high}F4/80^{high}$ red pulp macrophages (RPMs) in the spleen to internalize labeled ACs one hour after injection (**Fig. 1d**). These findings provide the first *in vivo* genetic evidence of the pivotal role of Gls1-dependent glutaminolysis during macrophage phagocytic clearance.

To determine the relevance of these observations during disease, we next tested Gls1 requirement in a mouse model of pathological atherosclerosis, in which defective lesional dead cell clearance translates into unstable necrotic core within plaques (Kojima et al., 2017; Tabas, 2010). Taking advantage of publicly available gene expression dataset of high-fat diet (HFD) fed wild-type (WT) and ApoE-deficient mice (Grabner et al., 2009) and computation analysis of metabolic networks (Jha et al., 2015), we first observed a downregulation of Gls1 expression in whole atheromatous plaques that was part of a global metabolic transcriptome signature making up a densely connected core that governs atherosclerotic lesions (**Fig. S2a**). Lower Gls1 expression correlated with an imbalance in markers of classically and alternatively activated macrophages and was inversely correlated to main characteristic of lipid-laden atherosclerotic plaques (i.e, CD36, ABCA1 and ABCG1 expression) (Heatmap, **Fig. S2a**). To monitor glutaminolysis activity in atherosclerotic plaque, we next investigated radiolabeled [^{14}C] glutamine uptake and hydrolysis in aortas extracted from WT and $ApoE^{-/-}$ mice fed on western diet (WD) for 6 weeks. Biomolecular imaging revealed higher glutamine incorporation into Oil Red O^{+} atherosclerotic prone areas, that were enriched in macrophages (**Fig. S2b**).

Nevertheless, quantification of [^{14}C] glutamine conversion into glutamate, after separation by thin-layer chromatography, confirmed lower glutaminase-dependent metabolism in atherosclerotic aorta (**Fig. S2c**). Next, Mac$^{\Delta Gls1}$ mice were crossed onto an atherosclerotic ApoE$^{-/-}$ background. After Western-type diet feeding (12 weeks), there was an approximately 1.7-fold increase in atherosclerosis plaque area in their proximal aortas compared to co-housed control littermates (**Fig. 2a**). Oil red O staining in aortas confirmed higher lipid-rich atherosclerotic plaques in ApoE$^{-/-}$ Mac$^{\Delta Gls1}$ mice (**Fig. 2b**) despite similar plasma lipid levels (**Fig. S2d**). Increased plaque area was also visualized in an independent cohort of ApoE$^{-/-}$ Mac$^{\Delta Gls1}$ mice using non-invasive ultrasound imaging (**Fig. 2c**). These effects were specific to macrophage glutaminolysis since hematopoietic Gls1-deficiency (i.e, generation of Mx1-Cre x Gs1$^{fl/fl}$ mice onto the atherosclerotic ApoE$^{-/-}$ background) recapitulated similar accelerated atherosclerosis than control animals (**Fig. S2e**). Further characterization of atherosclerotic lesions in ApoE$^{-/-}$ Mac$^{\Delta Gls1}$ mice revealed complex plaques containing macrophages (**Fig. S2f**) and necrotic core typified by a greater proportion of TUNEL-positive ACs and reduced ratio of macrophage associated to free AC, a hallmark of defective efferocytosis (**Fig. 2d**). We did not observe significant change in Ki67-positive proliferative cells in ApoE$^{-/-}$ Mac$^{\Delta Gls1}$ mice (**Fig. S2f**). To further support our hypothesis, we *i.p.* injected ApoE$^{-/-}$ Mac$^{\Delta Gls1}$ mice with fluorescent dye labeled apoptotic lymphocytes and examined macrophage efferocytic capacity one hour later. We confirmed the reduced ability of peritoneal macrophages from ApoE$^{-/-}$ Mac$^{\Delta Gls1}$ mice to phagocytose labeled ACs (**Fig. S2g**). To examine clinical significance, we investigated whether Gls1 expression correlated with human atherosclerotic plaque complexity. We found a reduced Gls1 expression in unstable *vs.* stable human carotid artery plaque. Moreover, we established a specific correlation between Gls1 expression and the M2-specific marker Arg1^{+} and an inverse correlation with plaque size, intraplaque hemorrhage (IPH) and necrotic core composition (**Fig. 2e**). Taken together, these results demonstrate that Gls1 contributes to AC engulfment in the pathological process of human and murine atherosclerosis.

To evaluate how IL-4 might couple macrophage glutaminolysis to efferocytosis, we performed an RNA sequencing (RNA-seq) analysis of PCMs after IL-4 complex *i.p* injection. When compared to control PCMs, Gls1-deficient cells had similar transcriptional regulation of genes involved in the sensing of soluble mediators released by ACs ('smell' or 'find-me' signals), the direct contact and recognition of ACs by ligand-receptor interactions ('taste' or 'eat me' signals) and the corpse internalization and processing ('ingestion' and 'digestion' processes) (Han and Ravichandran, 2011) (**Fig. S3a**). Consistently, inversion of alternatively activated controls and Mac$^{\Delta Gls1}$ BMDMs culture media at the initiation of efferocytosis had no impact on AC uptake excluding a role for the generation of an autocrine 'find-me' signal sensors (**Fig. S3b**). Further, alternatively activated Mac$^{\Delta Gls1}$ BMDMs treated only with AC supernatants exhibited similar percentage of fluorescent bead incorporation than control macrophages (**Fig. S3c**). We also investigated whether glutamine or glutamate uptake could serve as a 'smell' signal per se for surrounding cells as recently observed for glucose by-products (Morioka et al., 2018). The similar incorporation of [^{14}C] glutamine in presence or absence of competition with cold glutamine in alternatively activated Mac$^{\Delta Gls1}$ BMDMs first suggested similar glutamine sensing in these cells (**Fig. S3d**). Switching alternatively activated control and Gls1-deficient BMDMs to glutamine or glucose-free medium at the initiation of efferocytosis did not reduce uptake of ACs ruling out this hypothesis (**Fig. S3e**). Nevertheless, we found that intracellular Gls1 mRNA expression was similarly upregulated by IL-4 stimulation or AC ingestion in a validated gene expression dataset (Bosurgi et al., 2017) (**Fig. S3f**). We confirmed this upregulation in a time course experiment (**Fig. S3g**), paralleling a drop in cellular glutamine to glutamate ratio (**Fig. S3h**). We compared the accumulation of fluorescent apoptotic debris 30 min and 6 hours post-efferocytosis. Similar amount of fluorescent apoptotic debris was observed in alternatively activated Mac$^{\Delta Gls1}$ BMDMs compared to controls at 6 hours (**Fig. S3i**), indicating that perturbation in digestion efficiency was unlikely the culprit of the reduced efferocytosis. To distinguish fully internalized from partially engulfed ACs, we next incubated macrophages with prelabeled ACs and after 45 min, sealed and unsealed ACs were detected by CD4/CD8 staining before and after permeabilization, respectively (**Fig. S3j**). We found similar fraction of

$CD4^+CD8^+$ ACs in permeabilized control and Gls1-deficient macrophages but a lower fraction of $CD4^+CD8^+$ ACs in unpermeabilized alternatively activated $Mac^{\Delta Gls1}$ BMDMs, suggesting a defect in the energy-intensive dynamic actin rearrangements to engulf corpse rather than in phagosome sealing (**Fig. 3a**). Consistent with our hypothesis, transmission electron microscopy revealed less membrane ruffling surrounding the $Mac^{\Delta Gls1}$ BMDMs (**Fig. 3b**). Finally, phalloidine (red) immunostaining, 45 min after efferocytosis, revealed a general decrease in the amount of F-actin staining at the leading edge of membrane ruffle formation surrounding the apoptotic cells (green) (**Fig. 3c**). Thus, we identify that glutaminolysis meets the demand for high energy cytoskeletal rearrangement that facilitates the process of corpse engulfment.

To identify glutamine-dependent pathways that support the energy-intensive engulfment process, we traced ^{13}C-labeled glutamine intracellular fate and quantified several metabolites and by-products by liquid chromatography-mass spectrometry. Labeling distribution analyses revealed similar labeling of BC-AA in alternatively activated $Mac^{\Delta Gls1}$ BMDMs within 4 hours of addition of ^{13}C-glutamine (**Fig. 3d**). Consistently, similar amount of BB-AAs, such as leucine and valine, were observed in basal and alternatively activated $Mac^{\Delta Gls1}$ BMDMs (**Fig. S3k**). Consistent with these findings, inhibition of branched chain aminotransferases (BCATs) using Gabapentin (pan competitive inhibitor) or BCATc (BCAT2 selective inhibitor) was insufficient to restore the defective OCR and efferocytic function of alternatively activated $Mac^{\Delta Gls1}$ BMDMs (**Fig. S3l**). We next focused on the urea cycle pathway (**Fig. S3m**). A significant accumulation of unlabeled glutamyl-5-semi-aldehyde (GSA) (**Fig. 3d**) and pyrroline-5-carboxyllate (P5C) (**Fig. S3n**) in alternatively activated $Mac^{\Delta Gls1}$ BMDMs suggested a slower urea cycle turnover. However, we observed similar ^{13}C labeling in urea cycle metabolites (arginine and ornithine), proline or the N-acetylglutamate (NAG) intermediate in these cells (**Fig. 3d**). Quantification of urea cycle metabolites and by-products confirmed these findings (**Fig. S3n**) and ornithine supplementation to feed the urea cycle was not sufficient to rescue the OCR and efferocytosis of $Mac^{\Delta Gls1}$ BMDMs (**Fig. S3o**). Thus, neither higher BCAA catabolism or slower urea cycle turnover could explain the lower energy-dependent engulfment process of Gls1-deficient macrophages. In contrast, lower ^{13}C incorporation into TCA metabolites (succinate, malate, aconitase) and ATP in alternatively activated $Mac^{\Delta Gls1}$ BMDMs within 4 hours of addition of ^{13}C-glutamine supported partially defective TCA cycling in these cells (**Fig. 3d**). Consistently, we provide genetic evidence of reduced basal oxygen consumption rate (OCR) and maximal respiration after FCCP (carbonyl cyanide 4-[trifluoromethoxy] phenylhydrazone) treatment in $Mac^{\Delta Gls1}$ PCMs and BMDMs in comparison to control cells (**Fig. S3p and S3q**). These effects occurred independently of fluctuation in extracellular acidification rate (ECAR), a surrogate of glycolytic activity (**Fig. S3r**). We next addressed whether glutaminolysis could impact OXPHOS after ingestion of ACs. Flux measurements showed that both unstimulated and alternatively activated $Mac^{\Delta Gls1}$ BMDMs that were fed ACs, exhibited a decrease in maximal respiration response (**Fig. 3e and 3f**). These effects were also associated with a drop in ATP production reflecting an inability of these cells to respond to increased energy demand (**Fig. S3s**). Similar to IL-4 stimulation, basal OCR and maximal respiration response were also reduced during continued clearance of ACs (**Fig. 3g**). The decrease in mitochondria metabolism was also associated to higher total and mitochondrial ROS levels in both unstimulated and alternatively activated $Mac^{\Delta Gls1}$ BMDMs (**Fig. S3t**) suggesting a reverse electron transport (RET) by the mitochondrial electron transport chain (ETC). To dissect the origin of the defective OCR in Gls1-deficient macrophages and its causal role on efferocytosis, we used ETC pharmacological inhibitors or we supplemented $Mac^{\Delta Gls1}$ BMDMs with mitochondrial ROS scavengers (**Fig. 3h**). Indeed, mitochondrial redox status has been previously shown to metabolically pre-program macrophage skewing (Jais et al., 2014; Vats et al., 2006). Mitochondrial ROS scavenging by the superoxide dismutase mimetic (Tempol) or the mitochondria-targeted antioxidant coenzyme Q10 (MitoQ) was insufficient to rescue the defective OCR of alternatively activated $Mac^{\Delta Gls1}$ BMDMs, suggesting that mitochondrial ROS production are unlikely the cause but rather the consequence of the metabolic rewiring (**Fig. 3i**). These treatments did also not improve the efferocytic index in $Mac^{\Delta Gls1}$ BMDMs (**Fig. 3j**). We rather observed that direct OCR inhibition by targeting mitochondrial complex II (i.e,

succinate dehydrogenase (SDH)) with 3-Nitropropionic acid (3NPA) or complex III with antimycin A reduced efferocytosis in control cells to the levels of alternatively activated Mac$^{\Delta Gls1}$ BMDMs (**Fig. 3j**). Similar findings were observed during continued clearance of ACs (**Fig. S3u**). Consistent with the reduced OCR and pro-inflammatory properties of Risp knockout macrophages (Zhang et al., 2019), we also confirmed the genetic requirement of complex III to efferocytosis and continued clearance of ACs (**Fig. S3v**). Together, these findings reveal that glutaminolysis couples mitochondrial oxidative phosphorylation to ATP production for efficient efferocytosis.

We next compared differentially expressed genes in alternatively activated Mac$^{\Delta Gls1}$ PCMs to differentially expressed genes in macrophages that have engulfed ACs from a publicly available gene expression dataset (Morioka et al., 2018). Venn diagram revealed a core signature of genes that was commonly regulated by Gls1 deficiency and efferocytosis (**Fig. S4a**). Functional annotation enrichment analysis for GO terms highlighted mitochondria and redox status gene signatures (**Fig. S4a**) that are known to be exquisitely intertwined (Chandel, 2015; O'Neill and Pearce, 2016). Consistently, metabolic pathway enrichment analysis in resting and alternatively activated Mac$^{\Delta Gls1}$ PCMs highlighted down-regulation of KEGG pathways involved in oxidative phosphorylation and GSH synthesis (i.e, NADP, folate and GSH metabolism) (**Fig. S4b**). To dissect the interplay between the mitochondrial metabolic repurposing and the perturbation in antioxidant metabolism in Mac$^{\Delta Gls1}$ macrophages, we performed topological analyses using CoMBI-T profiling analysis (Jha et al., 2015) and compared the predictions to DreamBio that allows direct computational KEGG pathway mapping. CoMBI-T and DreamBio profiling analyses suggested that Mac$^{\Delta Gls1}$ PCM mitochondrial metabolic reprogramming could be linked directly to lower expression of tricarboxylic acid (TCA) cycle and aspartate-arginino-succinate (AAS) shunt genes that are interconnected to glutamine metabolism itself, carbohydrate, hexosamine and fatty acid metabolism (**Fig. 4a and S4c**). CoMBI-T predictions also revealed that the redox status of alternatively activated Mac$^{\Delta Gls1}$ PCMs could be linked to the one carbon cycle-centered module known to support the transsulfuration pathway (i.e, GSH synthesis) (**Fig. 4a**). KEGG mapping with DreamBio offered an alternative visualization of the perturbed transcriptomic pathways in alternatively activated Gls1-deficient macrophages and highlighted additional reactions that are not yet predicted to be connected (**Fig. S4c**). For instance, in contrast to CoMBI-T, DreamBio analysis predicted downregulation of phosphogluconate dehydrogenase (PGD) and malic enzyme (ME1) in alternatively activated Gls1-deficient macrophages. These are two key enzymes that also contribute to NADPH generation to efficiently supply reduced glutathione and maintain macrophages redox status (**Fig. S4c**). Consistent with these observations, the ratio between GSH (reduced glutathione)/GSSG (glutathione disulfide), known to scavenge reactive oxygen species (ROS) (DeBerardinis and Cheng, 2010), was greatly reduced in resting and alternatively activated Mac$^{\Delta Gls1}$ PCMs (**Fig. S4d**). Although total glutathione concentration was decreased to some extent in alternatively activated Mac$^{\Delta Gls1}$ PCMs, the decrease in the NADPH/NADP ratio was more strongly correlated to the GSH/GSSG ratio in resting and alternatively activated Mac$^{\Delta Gls1}$ PCMs (**Fig. S4d**). Altogether, this unique approach helped pinpoint the metabolic origin on how Gls1-dependent glutamine metabolism integrates canonical mitochondrial reprogramming and non-canonical redox status.

We first explored the canonical glutaminolysis pathway that relies on glutamate dehydrogenase (Glud1) to convert glutamate into α-ketoglutarate (α–KG) to fuel the TCA cycle. First, there was no difference in α-KG carbon numbers that originated from ^{13}C-glutamine in alternatively activated Mac$^{\Delta Gls1}$ BMDMs in comparison to the strong decrease detected in malate (**Fig. 3d**). Similar α-KG levels were also observed between controls and Mac$^{\Delta Gls1}$ BMDMs in our metabolomic analysis (data not shown). Consistent with these findings, treatment of control and Mac$^{\Delta Gls1}$ BMDMs with dimethyl α–KG did not rescue the inhibitory effect of Gls1 deficiency or BPTES (a Gls1 inhibitor) on basal OCR (**Fig. S4e**). α–KG-dependent KDM6 and ten-eleven translocation dioxygenase 2 (TET2) activities were also similar between control and Mac$^{\Delta Gls1}$ BMDMs (**Fig. S4f**) and similar expression of KDM6 target genes such as Phf2, Phf8, Jarid2 or

Mina were observed in these cells (**Fig. S4g**). Additionally, treatment of alternatively activated $Mac^{\Delta Gls1}$ BMDMs with a histone demethylase JMJD3 inhibitor (GSK-J4) or a broader DNA methyltransferase inhibitor (azacytidine) did not restore their OCR defect and particularly efferocytosis (**Fig. S4h**). Finally, similar global histone trimethylation modification, assessed by flow cytometry using H3K4me3 and H3K27me3 staining, was observed between controls and $Mac^{\Delta Gls1}$ BMDMs (**Fig. S4i**) and we did not find major transcriptional perturbation of epigenetic enzymes in Gls1-deficient macrophages (**Fig. S4j**). To confirm that α–KG generation through Glud1 was not responsible of the effects observed in Gls1-deficient macrophages, we generated myeloid specific Glud1-deficient mice ($HSC^{\Delta Glud1}$) (**Fig. 4b**). Unexpectedly, higher basal OCR and maximal respiration response (**Fig. 4c**), ATP production rate (**Fig. 4d**) and efferocytosis (**Fig. 4e**) were observed in alternatively activated macrophages genetically deficient in Glud1. An increase in glutathione concentration was also observed in these cells (data not shown). RNA sequencing analysis and functional annotation enrichment analysis for GO terms confirmed changes in transcriptional programs in Glud1-deficient macrophages, including enhanced immune process, whole membrane, cell activation or defense response (**Fig. 4f**). These findings suggest that Glud1 inhibition could redirect glutamate flux to promote efficient mitochondrial reprogramming and support the high energy requirement of efferocytosis. Inhibition of Glud1 with epigallocatechin gallate (EGCG) also exhibited an opposite effect versus Gls1 deficiency with increases in basal OCR and efferocytosis in alternatively activated control macrophages, and to some extent in $Mac^{\Delta Gls1}$ BMDMs (**Fig. 4g**). Altogether, these data suggest that Gls1-deficient macrophages metabolize less glutamate through a non-canonical glutaminolysis pathway to limit the TCA cycle anapleurosis required for efficient efferocytosis.

Based on our topological analyses, we next scrutinized the balance between the utilization of glutamate into the non-canonical GSH synthesis pathway that could prevent ATP leakage by limiting the γ-glutamyl futile cycle or into the non-canonical transaminase-dependent malate-aspartate shuttle that is nested to the AAS shunt to maximize the number of ATP molecules produced in mitochondria (DeBerardinis and Cheng, 2010) (**Fig. 5a**). We first excluded a role of the γ-glutamyl futile cycle in facilitating ATP leakage as we observed similar amount of the pyroglutamate intermediate (also known as PCA or 5-oxoproline) in $Mac^{\Delta Gls1}$ BMDMs despite reduced cystathionine levels (**Fig. S5a**). Treatment with N-acetylcysteine (NAC) to replenish this futile cycle and boost GSH synthesis had also no effect on OCR and efferocytosis in $Mac^{\Delta Gls1}$ BMDMs (**Fig. S5b**). In contrast, scavenging of ROS by direct supplementation of glutathione monoethyl ester (GSH) (**Fig. S5c**) raised basal OCR levels, ATP production and efferocytosis in alternatively activated $Mac^{\Delta Gls1}$ BMDMs to the levels of control macrophages (**Fig. 5b**). These findings suggest that GSH could overcome the perturbation of GSH salvage pathway (i.e, NADPH-producing pathways to recycle GSSG into GSH) in Gls1-deficient macrophages rather than limiting the γ-glutamyl futile cycle. There are several mechanisms of generating NADPH that depend on enzymes present in mitochondria including isocitrate dehydrogenase or malic enzyme. Topological analysis suggested a role of the malate-pyruvate cycling pathway (i.e, reduced ME1 expression) in $Mac^{\Delta Gls1}$ PCMs that directly relies on the malate-aspartate shuttle. Thus, we next inhibited the aspartate aminotransferases (GOT_s)-dependent transamination with aminooxyacetic acid (AOA) (**Fig. 5a**). Interestingly, AOA treatment reduced not only GSH levels (**Fig. S5c**) but also basal OCR and this limited efferocytosis in control macrophages to the levels of alternatively activated $Mac^{\Delta Gls1}$ BMDMs (**Fig. 5c**). Treatment with AOA also inhibited efferocytosis during continued clearance of ACs in control and $Mac^{\Delta Gls1}$ BMDMs (**Fig. S5d**). We validated these observations by showing that reduced expression of Got1 and Got2 by siRNA in BMDMs prevented the engulfment of apoptotic cells (**Fig. S5e**). Finally, AOA treatment also reversed the enhanced efferocytosis observed in alternatively activated Glud1-deficient BMDMs (**Fig. 5d**). Our results reveal that glutaminolysis and non-canonical transaminase pathways are preferentially used to maximize the number of ATP molecules produced in mitochondria for macrophage clearance function, which is linked to the ability of these pathways to power cells with the reducing equivalents necessary to detoxify ROS.

The energy-intensive cytoskeletal rearrangement to engulf corpse may rely on actin dynamics and these processes can be regulated by polymerization and depolymerization steps that can be accelerated by an ATP-dependent nucleation phase of new actin filaments or by small GTPases such as Rac1 and Cdc42 (Caron et al., 1998) (**Fig. S5f**). We indeed observed a slower polarization of G- to F-actin in alternatively activated $Mac^{\Delta Gls1}$ macrophages (**Fig. 5e**). Expression analysis of F-actin dynamic regulators did not reveal major differences in alternatively activated $Mac^{\Delta Gls1}$ PCMs, except thymosin beta-10 (Tmsb10) (**Fig. S5g**), a peptide that binds to ATP-containing actin monomers to limit actin nucleation. However, Tmsb10 protein expression was not altered in alternatively activated $Mac^{\Delta Gls1}$ macrophages (**Fig. S5h**). These findings indicate that transcriptional regulation was unlikely responsible for cytoskeletal rearrangement in Gls1 deficient macrophages. Because pull-down activation assay showed reduced activity of Cdc42 (**Fig. S5h**) and Rac1 (**Fig. S5i**) in alternatively activated $Mac^{\Delta Gls1}$ BMDMs, we next wondered if the conversion of ATP to GTP by mitochondrial nucleoside diphosphate kinase (Ndks) or succinyl-CoA ligases (Suclgs) could modulate small GTPase activity. Among these enzymes, expression of Nme1, Nme6 and Suclg1 was downregulated in alternatively activated $Mac^{\Delta Gls1}$ PCMs (**Fig. S5k**). Nevertheless, overexpression of Nme1/6 or Sucgl1 (**Fig. S5l**) was not sufficient to rescue the defective efferocytosis of alternatively activated $Mac^{\Delta Gls1}$ BMDMs (**Fig. S5m**).

Discussion

Macrophages need to handle a substantial amount of nutrients after ingestion of apoptotic cells (i.e, efferocytosis) to maintain normal tissue function (Han and Ravichandran, 2011). Especially, we and others have demonstrated that efferocytes can adapt their metabolism to face cholesterol and fatty acid overload during this process (A-Gonzalez et al., 2009)(Yvan-Charvet et al., 2010)(Viaud et al., 2018)(Zhang et al., 2019). Increased glucose uptake preceding AC engulfment could also prime continued AC clearance (Morioka et al., 2018). We now uncover that Gls1-dependent glutaminolysis is required to optimize AC clearance upon IL-4 stimulation or continued AC uptake by efficiently reprogramming macrophage metabolism. Indeed, conversion of glutamine through non-canonical transaminase pathways couples oxidative stress buffering to ATP production to meet the demand for high energy actin dyamics and cytoskeletal rearrangements.

Glutamine is considered a conditionally essential amino acid because of its role during conditions of metabolic stress, including injury (DeBerardinis and Cheng, 2010; O'Neill and Pearce, 2016). Glutamine utilization is increased in alternative macrophage polarization (Jha et al., 2015) and could predict macrophage activation profile in aortas of atherosclerotic mouse models (Tavakoli et al., 2017). However, the link between Gls1 and efferocytosis in this setting remains to be elucidated. Strikingly, despite enhanced glutamine utilization in the aortas of atherosclerotic mice, we observed impaired glutamate conversion and reduced Gls1 expression reflecting perturbed glutaminolysis. In our mouse and human datasets, we also observed that Gls1 expression within plaques was positively associated to canonical alternative polarization markers suggesting that glutaminolysis rather than glutamine uptake could predict macrophage profile. Functionally, we also observed that Gls1 expression negatively correlated to necrotic cores suggesting it could become a new imaging tool to assess defective efferocytosis as it is the case with ^{18}F-fluorodeoxyglucose PET imaging to detect inflamed tissues.

Modulation of glutamine metabolism at different steps can lead to strikingly different phenotypes. For instance, it has recently been suggested that glutaminolysis could support α–KG generation to orchestrate the jumonji domain containing-3 (Jmjd3, KDM6B)-dependent epigenetic reprogramming of alternatively activated macrophages *in vitro* (Liu et al., 2017) or promote mTORC1 signaling during Th1 differentiation (Jonhson et al., 2018). In the current setting, we neither observe perturbations of α–KG-dependent epigenetic reprogramming or upregulation of glycolysis and downstream mTOR signaling pathways in glutaminolysis deficient macrophages. Glutamine can be converted through at least two canonical and non-canonical mechanisms involving glutamate dehydrogenase (Glud1) or transaminases, respectively. Unexpectedly, Glud1 deficiency exhibited an opposite effect than Gls1 deficiency on efferocytosis suggesting that efferocytes metabolize glutamine in a manner that is different from the canonical α–KG generation model. Indeed, high-throughput transcriptional and metabolic profiling revealed that macrophage effector and clearance functions rely on a non-canonical transaminase pathway. The transaminase-dependent malate-aspartate shuttle is nested to the AAS shunt and requires glutamate to regenerate NADH, which is used to transfer electrons to the electron transport chain (ETC). This is required to maximize the number of ATP molecules produced in mitochondria and potentially favor NADPH production through ME-dependent malate-pyruvate cycling pathway to support GSH salvage pathway (DeBerardinis and Cheng, 2010). Consistently, all markers of these pathways were downregulated in Gls1-deficient macrophages. Although reduced GSH levels could explain the higher mitochondrial ROS in Gls1-deficient macrophages and mitochondrial redox status has been previously shown to metabolically pre-program macrophage skewing (Jais et al., 2014; Vats et al., 2006), we excluded a causal role of mitochondrial ROS in the metabolic reprogramming and defective efferocytosis of these cells using pharmacological mitochondrial ROS scavengers. Thus, treatment of Gls1-deficient macrophages with GSH most likely improved oxidative phosphorylation and efferocytosis by limiting NADPH consumption, which 'energy value' can be roughly estimated at between 2.5 and 3.5 ATP equivalents for purposes of comparing energy inputs and outputs of metabolic pathways (Stipanuk and Caudill, 2013). The central

role of ATP produced within mitochondria after glutamate is channeled into the malate-aspartate shuttle by aspartate aminotransferase (GOT)-dependent transamination in efferocytes was ultimately highlighted by directly targeting GOTs or mitochondrial complex II and III.

The metabolism of other amino acids has recently emerged to control macrophage effector functions. For example, BB-AAs cause itaconate accumulation, a hallmark of macrophage proinflammatory response (Papathanassiu et al., 2017)(O'Neill and Artyomov 2019). The group led by Tabas et al. have also recently reported that the metabolism of AC-derived arginine or ornithine to putrescine is required for continual efferocytosis by a mechanism involving cytoskeletal rearrangements (Yurdagul et al., 2020) and potentially linked to mitochondrial fission (Wang et al., 2017). This pathway is induced in alternatively activated macrophages (Jha et al., 2015), known to enhance efferocytic response for efficient tissue repair (Bosurgi et al., 2017). Impairment of macrophage glutaminolysis described here is predicted to occur independently of the aforementioned metabolic pathways as similar levels of BB-AAs and putrescine were observed in Gls1-deficient macrophages and inhibition of BCAT or ornithine supplementation did not rescue the defective efferocytosis of these cells. This pathway may contribute to daily clearance of billions of white blood cells to maintain tissue homeostasis as illustrated here in the liver, spleen and peritoneal cavity (Elliott and Ravichandran, 2016) or lead to impaired resolution and tissue necrosis as illustrated in progressing atherosclerosis (Kojima et al., 2017; Tabas, 2010).

The high energy demand for cytoskeletal rearrangements during efferocytosis has previously been suggested but the underlying mechanisms remain poorly understood (Elliott and Ravichandran, 2016). Most of the studies focus on small GTPase such as Rac1 or Cdc42 because they are key regulators of membrane ruffling for AC recognition and internalization (Han and Ravichandran, 2011). However, actin remodeling can also be directly regulated by polymerization and depolymerization steps that are energy-intensive processes. Along with reduced ATP production in Gls1-deficient macrophages, we observed both impaired actin polymerization and reduced Cdc42 and Rac1 activities. Although the link between ATP production and actin polymerization makes intuitive sense, the link with small GTPase activation is less apparent. Nevertheless, blockade of the AAS shunt to limit ATP production clearly recapitulated these observations. Because Rac1 was not regulated at the transcriptional levels, we reasoned that ATP production might directly be linked to GTP production to activate small GTPase (Boissan et al., 2018). However, we did not find evidences that conversion of ATP to GTP by Nme1/6 or Suclg1 could explain modulation of efferocytic response. It is possible that other mechanisms such as regulation of (GTP)-exchange factor (GEF) may be involved and future studies will be required to address this question (Marei and Malliri, 2017).

Collectively, our results reveal a novel dependence on transaminases for metabolism of the glutamine carbon skeleton during key macrophage effector functions that are required for tissue repair. Mechanistically, these reactions orchestrate ATP generation through the ETC in the presence of IL-4 or during continued apoptotic cell clearance. These findings support the larger concept that any process that compromises the metabolic reprogramming and ATP production of efferocytes will likely result in dire pathologic consequences. Conversely, therapeutic interventions to enhance macrophage glutaminolysis and boost efferocytosis may be able to face maladaptive inflammation and necrosis.

Figure 1

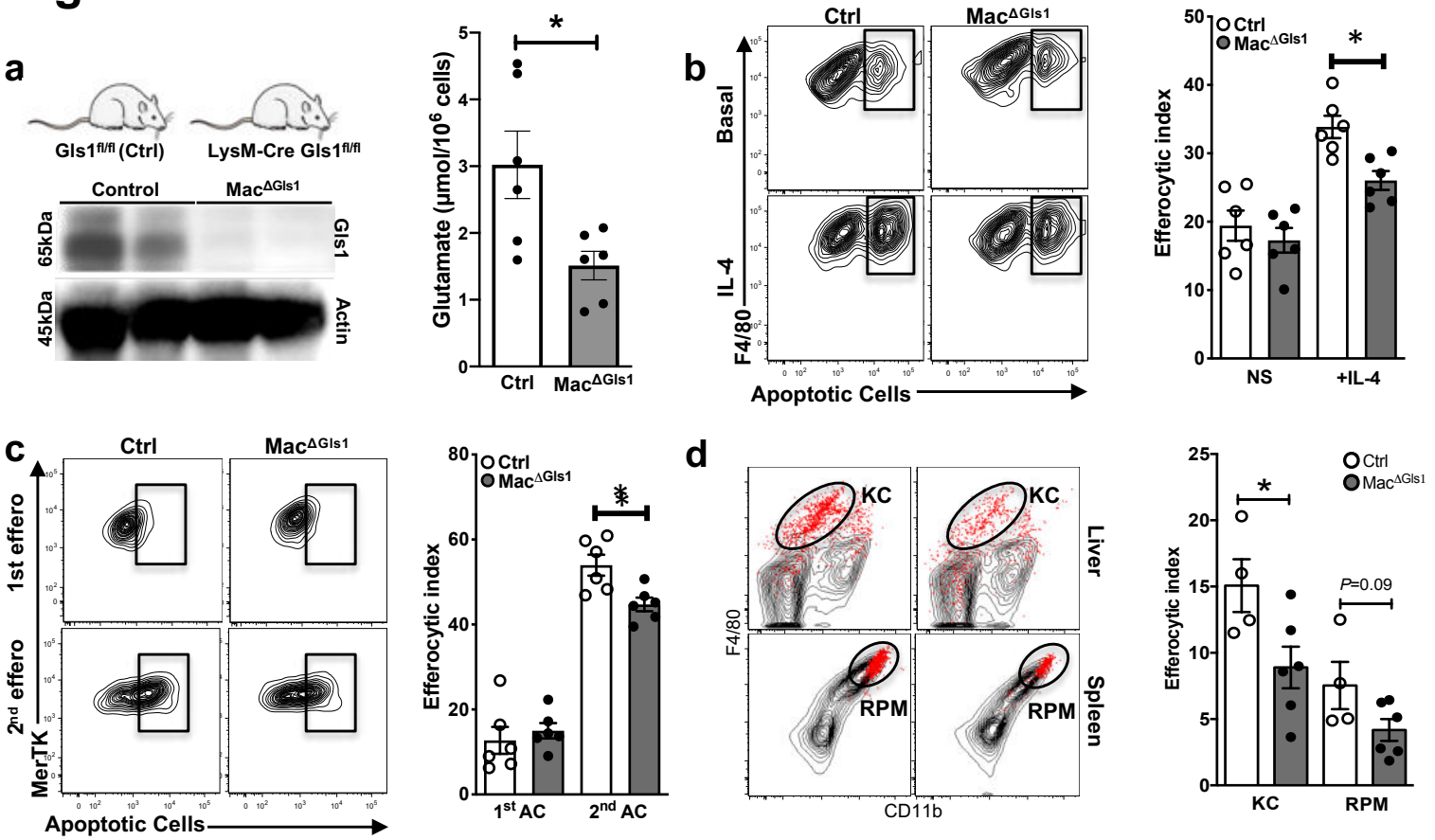

Figure 1: Macrophage-Gls1 deletion impairs efferocytosis *in vitro* and *in vivo*. (a) Western blot of Gls1 protein (left) and Glutamate levels (right) in Control or Mac$^{\Delta Gls1}$ PCMs. **(b)** Efferocytic index gating strategy (left) and quantification (right) measured by flow cytometry after 45min exposure with apoptotic cells (ACs) in BMDMs at steady state or after overnight IL-4 stimulation. Efferocytic index was calculated as follows: (number of macrophages with ACs/total number of macrophages) × 100. **(c)** Efferocytic index gating strategy (Left) and quantification (right) measured by flow cytometry after one (45min) or two (45min + 1-hour rest + 45min) incubations with ACs in control or Mac$^{\Delta Gls1}$ BMDMs. **(d)** Efferocytic index gating strategy (left) and quantification (right) measured by flow cytometry in control or Mac$^{\Delta Gls1}$ Kupffer cells (KC) and red pulp macrophages (RPM) after labelled apoptotic thymocytes i.v. injection. All values are mean ± SEM and are representative of at least one experiment (n=4-6 independent animals). **P*<0.05 *compared to control*.

Figure 2

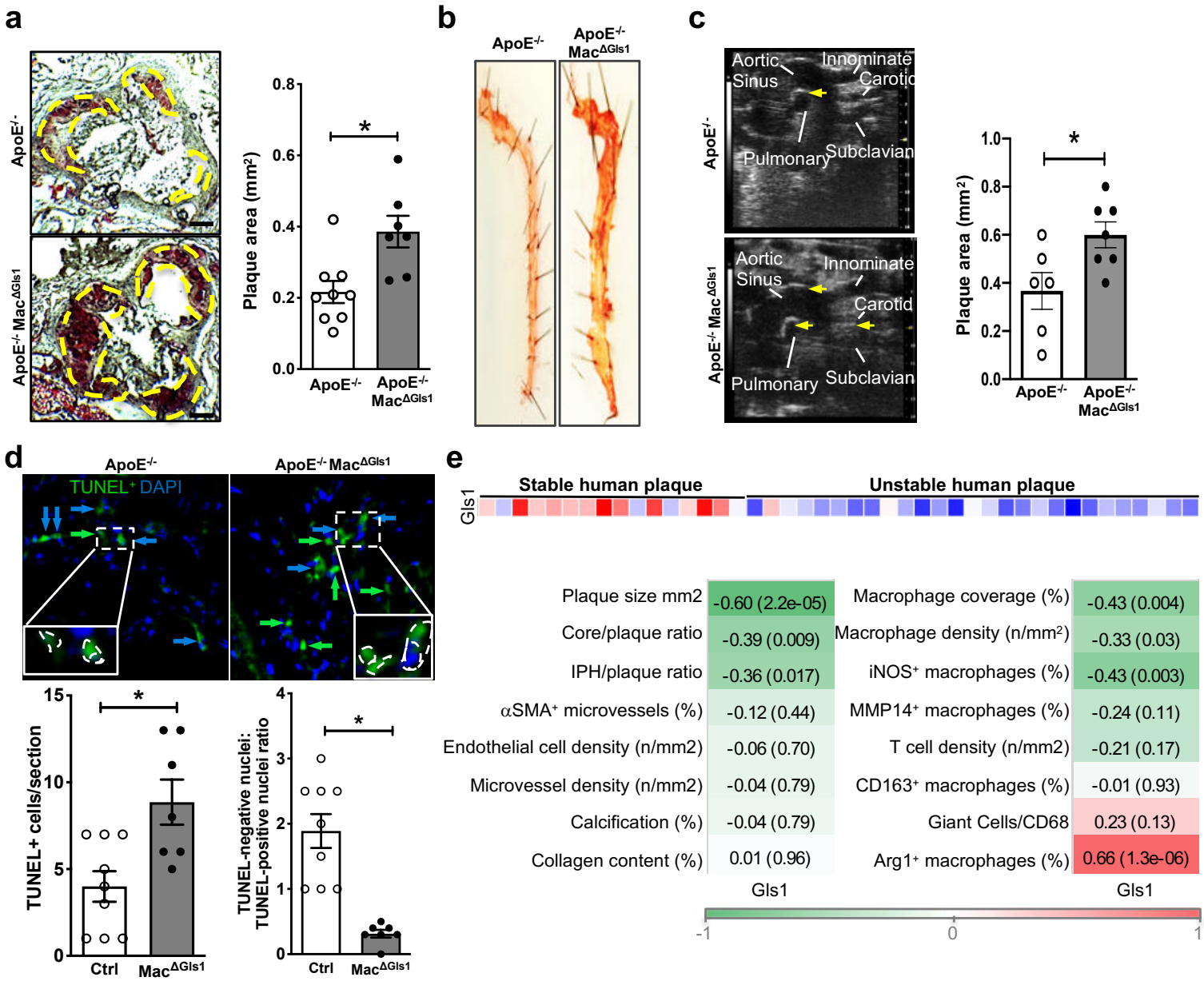

Figure 2: Myeloid-Gls1 deletion impairs efferocytosis in the pathological process of atherosclerosis. (a) Representative sections (left) and quantification (right) of aortic plaques from ApoE$^{-/-}$ or ApoE$^{-/-}$ Mac$^{\Delta Gls1}$ mice (12 weeks WD) stained for Oil Red O and Hematoxylin Eosin. Scale bar: 200□m. **(b)** Oil red O stained descending aortas from ApoE$^{-/-}$ or ApoE$^{-/-}$ Mac$^{\Delta Gls1}$ mice maintained on a WD for 12 weeks. **(c)** Echography (left) and quantification (right) of aortic plaques from ApoE$^{-/-}$ or ApoE$^{-/-}$ Mac$^{\Delta Gls1}$ mice fed for 12 weeks on WD. Arrows indicate plaque areas. **(d)** Representative images (top) and quantification (bottom) of TUNEL^{+} cells in aortic plaques from ApoE$^{-/-}$ or ApoE$^{-/-}$ Mac$^{\Delta Gls1}$ mice (12 weeks WD). Green and blue arrow depict TUNEL negative nuclei and TUNEL-positive nuclei, respectively. **(e)** Correlation between Gls1 expression and human atherosclerotic plaque complexity in the Maastricht Pathology collection. All values are mean ± SEM and are representative of at least one experiment (n=6-9). *P<0.05 *compared to control*.

Figure 3

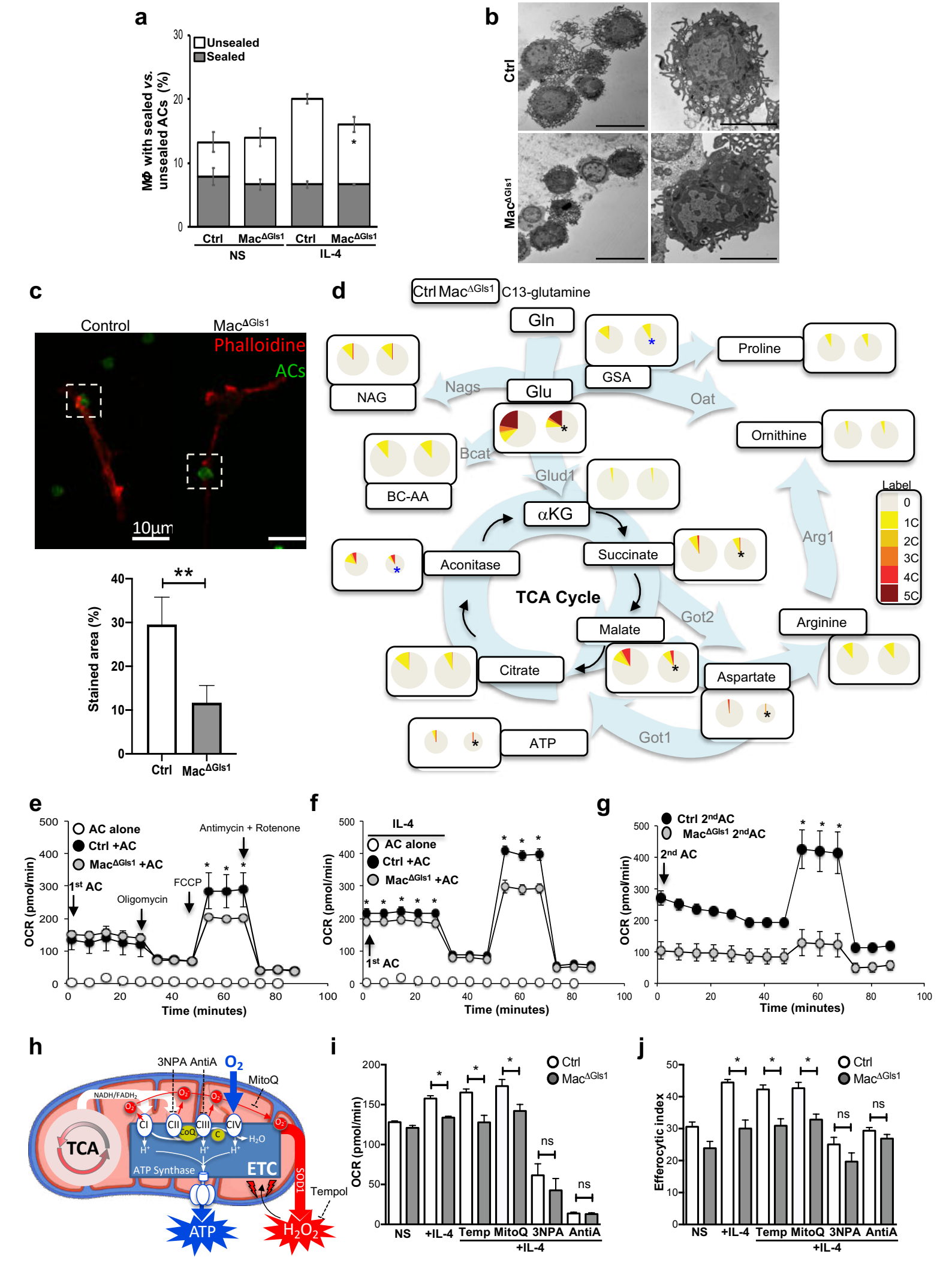
a
Unsealed
Sealed
MΦ with sealed vs. unsealed ACs (%)
Ctrl
MacΔGls1
Ctrl
MacΔGls1
NS
IL-4
b
Ctrl
MacΔGls1
c
Control
MacΔGls1
Phalloidine
ACs
10µm
Stained area (%)
Ctrl
MacΔGls1
d
Ctrl MacΔGls1 C13-glutamine
Gln
NAG
Nags
Glu
GSA
Proline
Oat
Ornithine
Bcat
BC-AA
Glud1
αKG
Aconitase
Succinate
Arg1
TCA Cycle
Got2
Malate
Arginine
Citrate
Aspartate
ATP
Got1
Label
0
1C
2C
3C
4C
5C
e
AC alone
Ctrl +AC
MacΔGls1 +AC
1st AC
Oligomycin
FCCP
Antimycin + Rotenone
OCR (pmol/min)
Time (minutes)
f
IL-4
AC alone
Ctrl +AC
MacΔGls1 +AC
1st AC
OCR (pmol/min)
Time (minutes)
g
Ctrl 2ndAC
MacΔGls1 2ndAC
2nd AC
OCR (pmol/min)
Time (minutes)
h
3NPA AntiA
O2
MitoQ
NADH/FADH2
CI
CII
CIII
CIV
CoQ
C
H2O
TCA
ATP Synthase
ETC
SOD1
Tempol
ATP
H2O2
i
Ctrl
MacΔGls1
OCR (pmol/min)
NS
+IL-4
Temp
MitoQ
3NPA
AntiA
+IL-4
ns
j
Ctrl
MacΔGls1
Efferocytic index
NS
+IL-4
Temp
MitoQ
3NPA
AntiA
+IL-4
ns

Figure 3 Glutamine metabolism supports the high energy requirement of efferocytosis. **(a)** Apoptotic cell internalization quantification in control or $Mac^{\Delta Gls1}$ PCMs stimulated overnight +/- IL-4. **(b)** Transmission electron microscopy imaging of control or $Mac^{\Delta Gls1}$ PCMs. Left scale bar: 10□m. Right scale bar: 5□m. **(c)** Representative images of control or $Mac^{\Delta Gls1}$ BMDMs stimulated overnight with IL-4 and stained for F-actin (Red) and ACs (green). Scale bar: 10µm. **(d)** Carbon fluxes using U-13C-glutamine. U-13C glutamine was added in the medium of non-stimulated and IL-4-treated macrophages. Circle sizes are scaled with respect to pool size for individual metabolites in each condition. Thin black arrows represent known metabolic pathway connections; background arrows indicate deduced major metabolic flows in alternatively activated macrophages. **(e)** OCR measured by Seahorse after one incubation with ACs in control or $Mac^{\Delta Gls1}$ BMDMs in basal conditions or **(f)** stimulated overnight with IL-4. **(g)** OCR measurement after two exposures with ACs in control or $Mac^{\Delta Gls1}$ BMDMs. **(h)** Schematic representation of mitochondria electron transport chain and its pharmacological inhibitors. **(i)** OCR quantification and **(j)** efferocytic index of control or $Mac^{\Delta Gls1}$ BMDMs at steady state or after overnight IL-4 stimulation +/- Tempol, Mitoquinol, 3NPA or antimicyn A. All values are mean ± SEM and are representative of at least one experiment (n=3-9). **P*<0.05 compared *to control*.

Figure 4

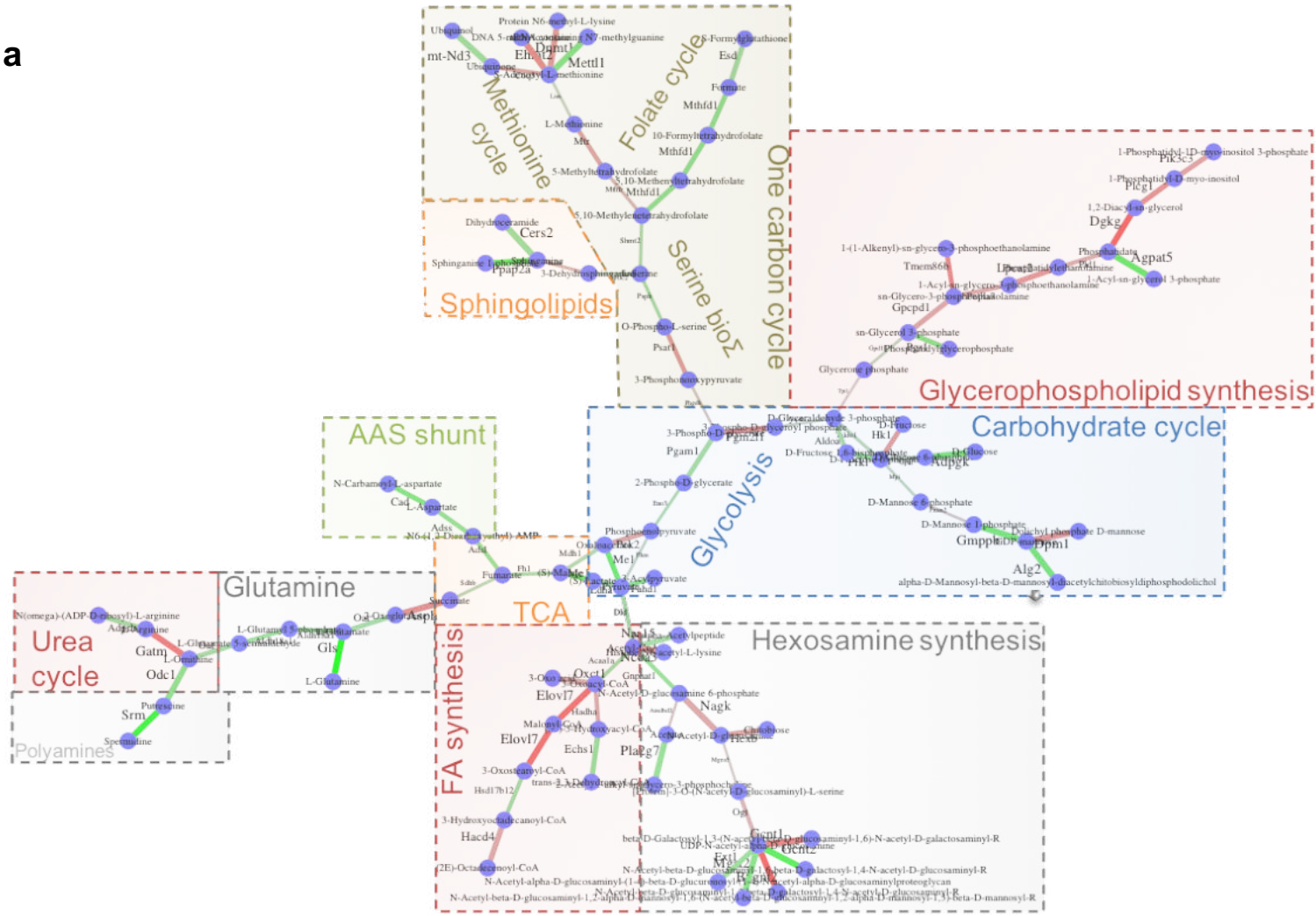
a
Methionine cycle
Folate cycle
One carbon cycle
Serine bioΣ
Sphingolipids
Glycerophospholipid synthesis
Carbohydrate cycle
AAS shunt
Glycolysis
Glutamine
Urea cycle
TCA
Polyamines
FA synthesis
Hexosamine synthesis

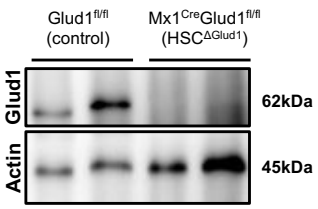
b
Glud1fl/fl (control)
Mx1CreGlud1fl/fl (HSCΔGlud1)
Glud1
Actin
62kDa
45kDa

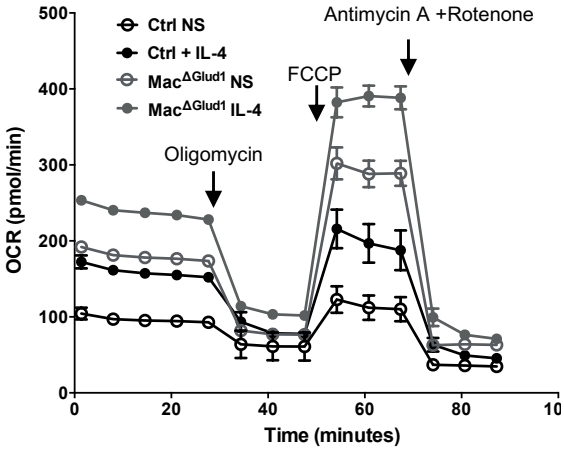
c
Ctrl NS
Ctrl + IL-4
MacΔGlud1 NS
MacΔGlud1 IL-4
Antimycin A +Rotenone
FCCP
Oligomycin
OCR (pmol/min)
Time (minutes)

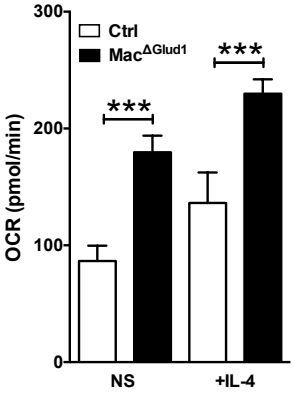
Ctrl
MacΔGlud1
OCR (pmol/min)
NS
+IL-4

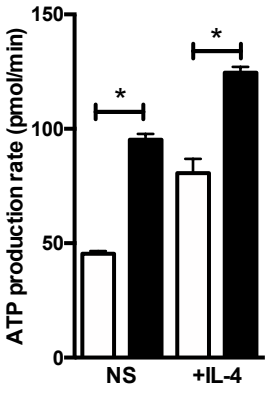
ATP production rate (pmol/min)
NS
+IL-4

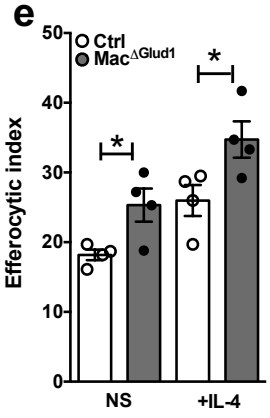
e
Ctrl
MacΔGlud1
Efferocytic index
NS
+IL-4

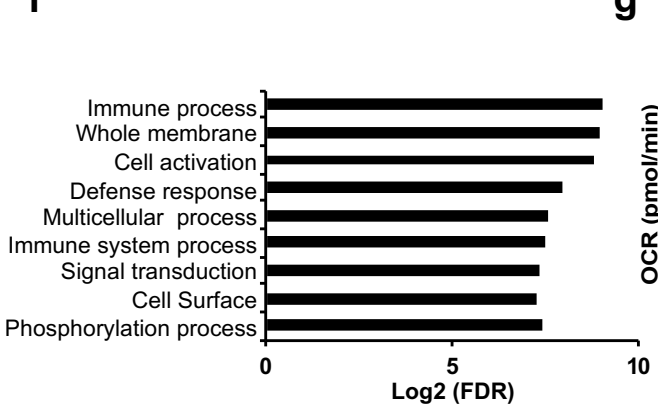
f
Immune process
Whole membrane
Cell activation
Defense response
Multicellular process
Immune system process
Signal transduction
Cell Surface
Phosphorylation process
Log2 (FDR)

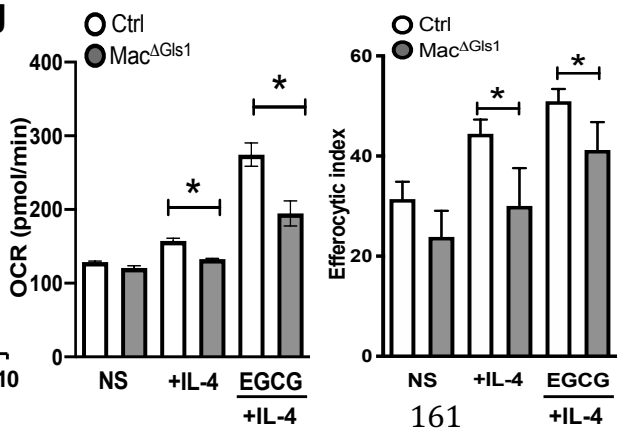
g
Ctrl
MacΔGls1
OCR (pmol/min)
NS
+IL-4
EGCG +IL-4
Efferocytic index

Figure 4: Macrophages utilize a non-canonical glutamine metabolism pathway to promote efficient efferocytosis. (a) CoMBI-T profiling analysis from RNAseq data of alternatively activated Gls1-deficient or sufficient PCMs. **(b)** Glud1 protein expression assessed by Western blotting in control or $HSC^{\Delta Glud1}$ PCMs. **(c)** OCR and **(d)** ATP production rate measured by Seahorse in control or $Mac^{\Delta Glud1}$ BMDMs at steady state or after overnight IL-4 stimulation. **(e)** efferocytic index in control or $Mac^{\Delta Glud1}$ BMDMs at steady state or after overnight IL-4 stimulation. **(f)** RNAseq analysis and functional annotation enrichment analysis for GO terms in control or $Mac^{\Delta Gls1}$ PCMs. **(g)** OCR quantification (left) and efferocytic index (right) from control or $Mac^{\Delta Gls1}$ BMDMs in basal conditions or overnight IL-4 stimulation +/- EGCG. All values are mean ± SEM and are representative of at least one experiment (n=3-8). **P*<0.05, ****P*<0.0005 compared *to control*.

Figure 5

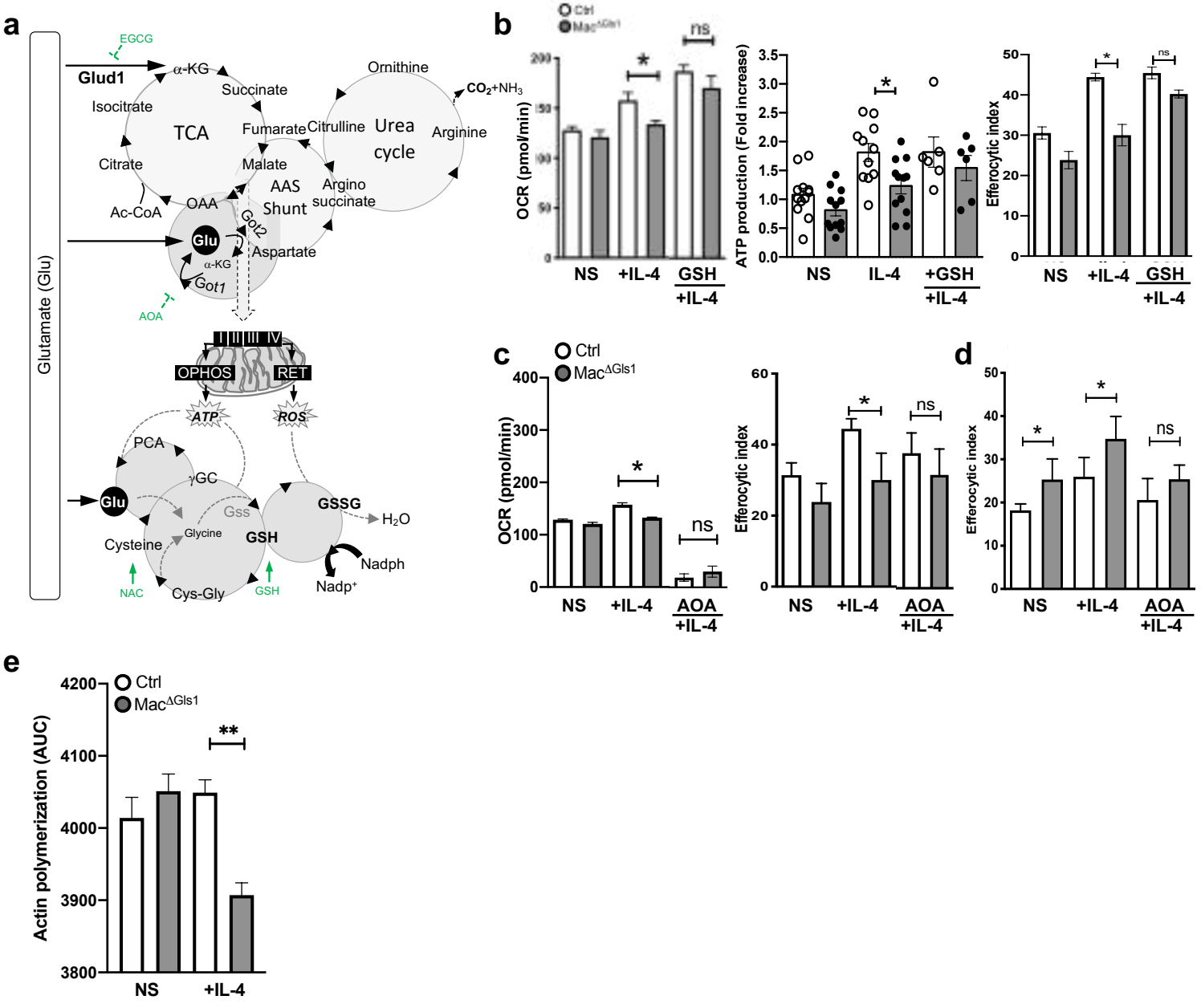

Figure 5: Non-canonical transaminase pathway supports glutamine carbon skeleton metabolism to promote cytoskeletal rearrangement and corpse engulfment. (a) Schematic representation of glutamate incorporation into metabolic cycles. **(b)** OCR quantification (left), ATP production (middle) and efferocytic index (right) in control or Mac$^{\Delta Gls1}$ BMDMs in basal conditions or overnight IL-4 stimulation +/- GSH. **(c)** OCR quantification (left) and efferocytic index (right) in control or Mac$^{\Delta Gls1}$ BMDMs in basal conditions or overnight IL-4 stimulation +/- AOA. **(d)** OCR quantification (left) and efferocytic index (right) in control or Mac$^{\Delta Glud1}$ BMDMs in basal conditions or overnight IL-4 stimulation +/- AOA. **(e)** Actin polymerization assay in control or Mac$^{\Delta Gls1}$ BMDMs in basal condition or following overnight IL-4 stimulation. All values are mean ± SEM and are representative of at least one experiment (n=3-12). *P<0.05 compared *to control*.

Figure S1

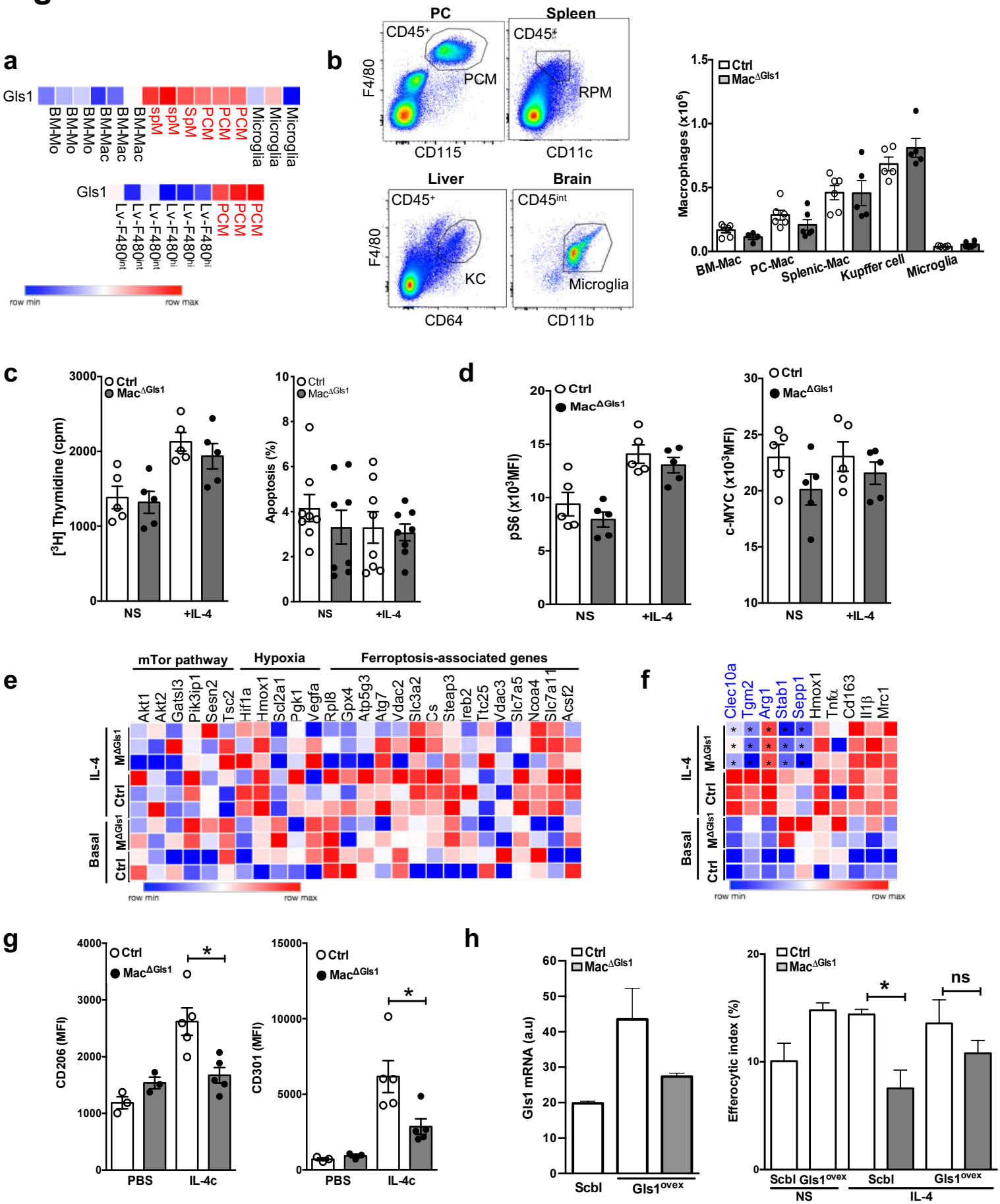
a
Gls1
BM-Mo
BM-Mo
BM-Mo
BM-Mac
BM-Mac
BM-Mac
spM
spM
SpM
PCM
PCM
PCM
Microglia
Microglia
Microglia
Gls1
Lv-F480int
Lv-F480int
Lv-F480int
Lv-F480hi
Lv-F480hi
Lv-F480hi
PCM
PCM
PCM
PCM
row min
row max
b
PC
Spleen
CD45+
CD45+
PCM
RPM
F4/80
CD115
CD11c
Liver
Brain
CD45+
CD45int
KC
Microglia
F4/80
CD64
CD11b
Ctrl
MacΔGls1
Macrophages (x10⁶)
BM-Mac
PC-Mac
Splenic-Mac
Kupffer cell
Microglia
c
Ctrl
MacΔGls1
[³H] Thymidine (cpm)
NS
+IL-4
Apoptosis (%)
d
pS6 (x10³MFI)
c-MYC (x10³MFI)
e
mTor pathway
Hypoxia
Ferroptosis-associated genes
Akt1
Akt2
Gatsl3
Pik3ip1
Sesn2
Tsc2
Hif1a
Hmox1
Scl2a1
Pgk1
Vegfa
Rpl8
Gpx4
Atp5g3
Atg7
Vdac2
Slc3a2
Cs
Steap3
Ireb2
Ttc25
Vdac3
Slc7a5
Ncoa4
Slc7a11
Acsf2
IL-4
Basal
MΔGls1
Ctrl
row min
row max
f
Clec10a
Tgm2
Arg1
Stab1
Sepp1
Hmox1
Tnfα
Cd163
Il1β
Mrc1
g
CD206 (MFI)
PBS
IL-4c
CD301 (MFI)
h
Gls1 mRNA (a.u)
Scbl
Gls1ovex
Efferocytic index (%)
ns
NS
IL-4

Figure S1: GLS1 is dispensable for macrophage homeostasis but supports macrophage effector and clearance functions. (a) Comparative analysis of Gls1 mRNA expression in different macrophage populations from a publicly available dataset (Immgen). **(b)** Macrophage population gating strategy (left) and numbers (right) measured by flow cytometry in multiple mouse tissues (bone marrow, peritoneal cavity, spleen, liver and brain). n= 5-6 **(c)** [^{3}H]-Thymidine incorporation (left) and apoptosis percentage (right) in control or Mac$^{\Delta Gls1}$ BMDMs at steady state or after an overnight stimulation with IL-4. **(d)** Phospho-S6 (left) and c-myc (right) expression measured by flow cytometry in control or Mac$^{\Delta Gls1}$ BMDMs with or without overnight IL-4 stimulation. **(e)** RNAseq of control or Mac$^{\Delta Gls1}$ cell sorted PCMs at steady state or after IL-4 stimulation. **(f)** RNAseq analysis with focus on alternatively activated genes in control or Mac$^{\Delta Gls1}$ PCMs stimulated overnight or not with IL-4. **(g)** CD206 and CD301 expression by flow cytometry in mice injected i.p. with PBS or IL-4-complex. **(h)** qPCR quantification (left) and efferocytic index (right) of Gls1 lentivirus overexpression in control or Mac$^{\Delta Gls1}$ BMDMs stimulated overnight with IL-4. All values are mean ± SEM and are representative of at least one experiment (n=3–13 independent animals). *P<0.05

Figure S2

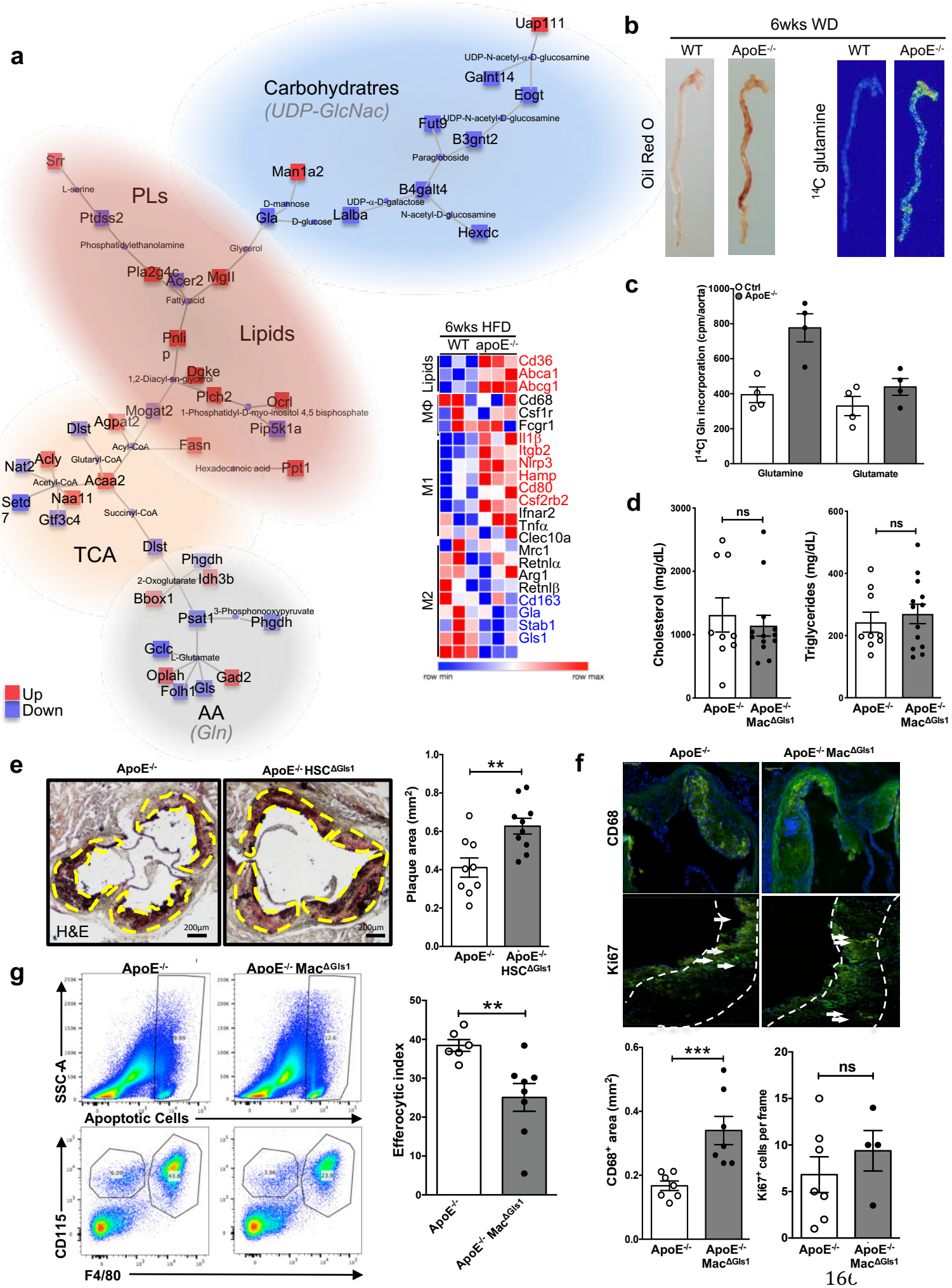
a
Carbohydratres
(UDP-GlcNac)
Uap111
UDP-N-acetyl-α-D-glucosamine
GalNt14
Eogt
UDP-N-acetyl-D-glucosamine
Fut9
B3gnt2
Paraglobioside
Man1a2
B4galt4
D-mannose
UDP-α-D-galactose
Gla
D-glucose
Lalba
N-acetyl-D-glucosamine
Hexdc
Srr
L-serine
PLs
Ptdss2
Phosphatidylethanolamine
Glycerol
Pla2g4c
Acer2
Mgll
Fatty acid
Lipids
Pnlip
Dgke
1,2-Diacyl-sn-glycerol
Plch2
Ocrl
1-Phosphatidyl-D-myo-inositol 4,5 bisphosphate
Mogat2
Dlst
Agpat2
Pip5k1a
Acyl-CoA
Fasn
Nat2
Acly
Glutaryl-CoA
Hexadecanoic acid
Ppt1
Acetyl-CoA
Acaa2
Setd7
Naa11
Gtf3c4
Succinyl-CoA
TCA
Dlst
Phgdh
2-Oxoglutarate
Idh3b
Bbox1
Psat1
3-Phosphonooxypyruvate
Phgdh
Gclc
L-Glutamate
Oplah
Gad2
Folh1
Gls
AA
(Gln)
Up
Down
6wks HFD
WT apoE-/-
Lipids
MΦ
M1
M2
Cd36
Abca1
Abcg1
Cd68
Csf1r
Fcgr1
Il1β
Itgb2
Nlrp3
Hamp
Cd80
Csf2rb2
Ifnar2
Tnfα
Clec10a
Mrc1
Retnlα
Arg1
Retnlβ
Cd163
Gla
Stab1
Gls1
row min
row max
b
6wks WD
WT
ApoE-/-
Oil Red O
14C glutamine
c
[14C] Gln incorporation (cpm/aorta)
Ctrl
ApoE-/-
Glutamine
Glutamate
d
Cholesterol (mg/dL)
Triglycerides (mg/dL)
ns
ApoE-/-
ApoE-/- MacΔGls1
e
ApoE-/-
ApoE-/- HSCΔGls1
H&E
200μm
Plaque area (mm2)
**
f
ApoE-/-
ApoE-/- MacΔGls1
CD68
Ki67
CD68+ area (mm2)
Ki67+ cells per frame
***
g
ApoE-/-
ApoE-/- MacΔGls1
SSC-A
Apoptotic Cells
CD115
F4/80
Efferocytic index

Figure S2: Atherosclerosis development relies on GLS1-dependent glutaminolyis. (a) Metabolic pathway (left) and RNAseq analysis (right) of ApoE$^{-/-}$ versus WT mouse aortas (6 weeks on WD) performed with Phantasus software (GSE10000). **(b)** Oil red O staining (left) or ^{14}C glutamine accumulation after i.v. injection (right) in descending aortas extracted from WT and ApoE$^{-/-}$ mice maintained on a WD for 6 weeks. **(c)** ^{14}C glutamine incorporation in aortas obtained from ApoE$^{-/-}$ and ApoE$^{-/-}$ Mac$^{\Delta Gls1}$ mice fed for 6 weeks on WD. **(d)** Cholesterol (left) and triglyceride (right) content in plasma of ApoE$^{-/-}$ and ApoE$^{-/-}$ Mac$^{\Delta Gls1}$ mice. **(e)** Representative sections (left) and quantification (right) of aortic plaques from ApoE$^{-/-}$ or ApoE$^{-/-}$ HSC$^{\Delta Gls1}$ mice (12 weeks WD) stained for Oil Red O and Hematoxylin Eosin. Scale bar: 200□m. **(f)** Representative sections (top) and quantification (bottom) of aortic plaques from ApoE$^{-/-}$ or ApoE$^{-/-}$ Mac$^{\Delta Gls1}$ mice (12 weeks WD) stained for CD68 and Ki67. **(g)** Gating strategy (left) and quantification (right) of PCM efferocytic index in ApoE$^{-/-}$ *and* ApoE$^{-/-}$ Mac$^{\Delta Gls1}$ mice 1-hour after labeled ACs i.p. injection. All values are mean ± SEM and are representative of at least one experiment (n=4–13). ***P*<0.005; ****P*<0.0005 compared *to control*.

Figure S3

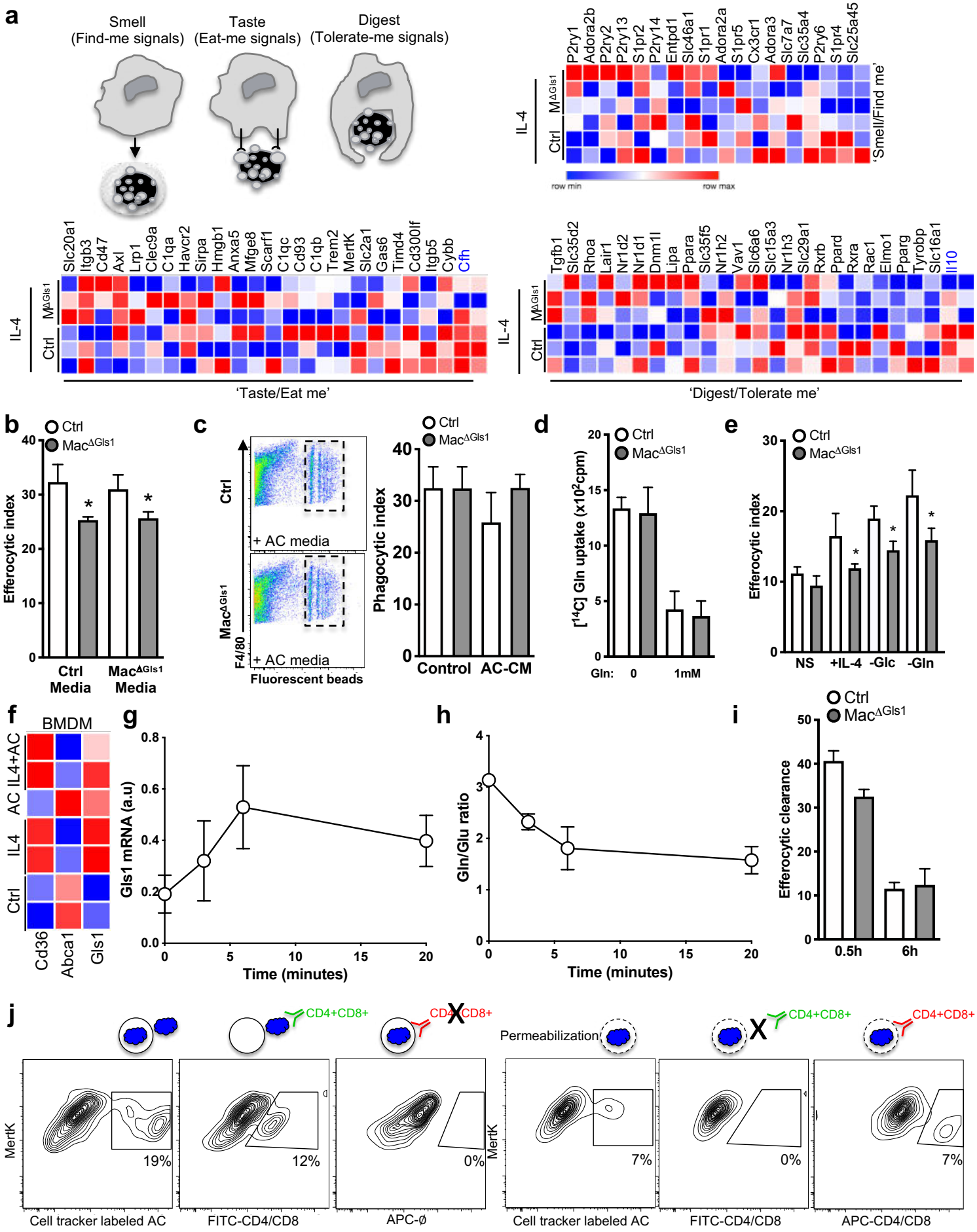
a
Smell
(Find-me signals)
Taste
(Eat-me signals)
Digest
(Tolerate-me signals)
P2ry1 Adora2b P2ry2 P2ry13 S1pr2 P2ry14 Entpd1 Slc46a1 S1pr1 Adora2a S1pr5 Cx3cr1 Adora3 Slc7a7 Slc35a4 P2ry6 S1pr4 Slc25a45
IL-4
MΔGls1
Ctrl
'Smell/Find me'
row min
row max
Slc20a1 Itgb3 Cd47 Axl Lrp1 Clec9a C1qa Havcr2 Sirpa Hmgb1 Anxa5 Mfge8 Scarf1 C1qc Cd93 C1qb Trem2 MertK Slc2a1 Gas6 Timd4 Cd300lf Itgb5 Cybb Cfh
'Taste/Eat me'
Tgfb1 Slc35d2 Rhoa Lair1 Nr1d2 Nr1d1 Dnm1l Lipa Ppara Slc35f5 Nr1h2 Vav1 Slc6a6 Slc15a3 Nr1h3 Slc29a1 Rxrb Ppard Rxra Rac1 Elmo1 Pparg Tyrobp Slc16a1 Il10
'Digest/Tolerate me'
b
Ctrl
MacΔGls1
Efferocytic index
Ctrl Media
MacΔGls1 Media
c
Ctrl
MacΔGls1
+ AC media
F4/80
Fluorescent beads
Phagocytic index
Control
AC-CM
d
[14C] Gln uptake (x10^2cpm)
Gln: 0 1mM
e
Efferocytic index
NS
+IL-4
-Glc
-Gln
f
BMDM
AC IL4+AC
IL4
Ctrl
Cd36
Abca1
Gls1
g
Gls1 mRNA (a.u)
Time (minutes)
h
Gln/Glu ratio
Time (minutes)
i
Efferocytic clearance
0.5h
6h
j
CD4+CD8+
Permeabilization
MertK
19%
12%
0%
7%
0%
7%
Cell tracker labeled AC
FITC-CD4/CD8
APC-Ø
APC-CD4/CD8

Figure S3

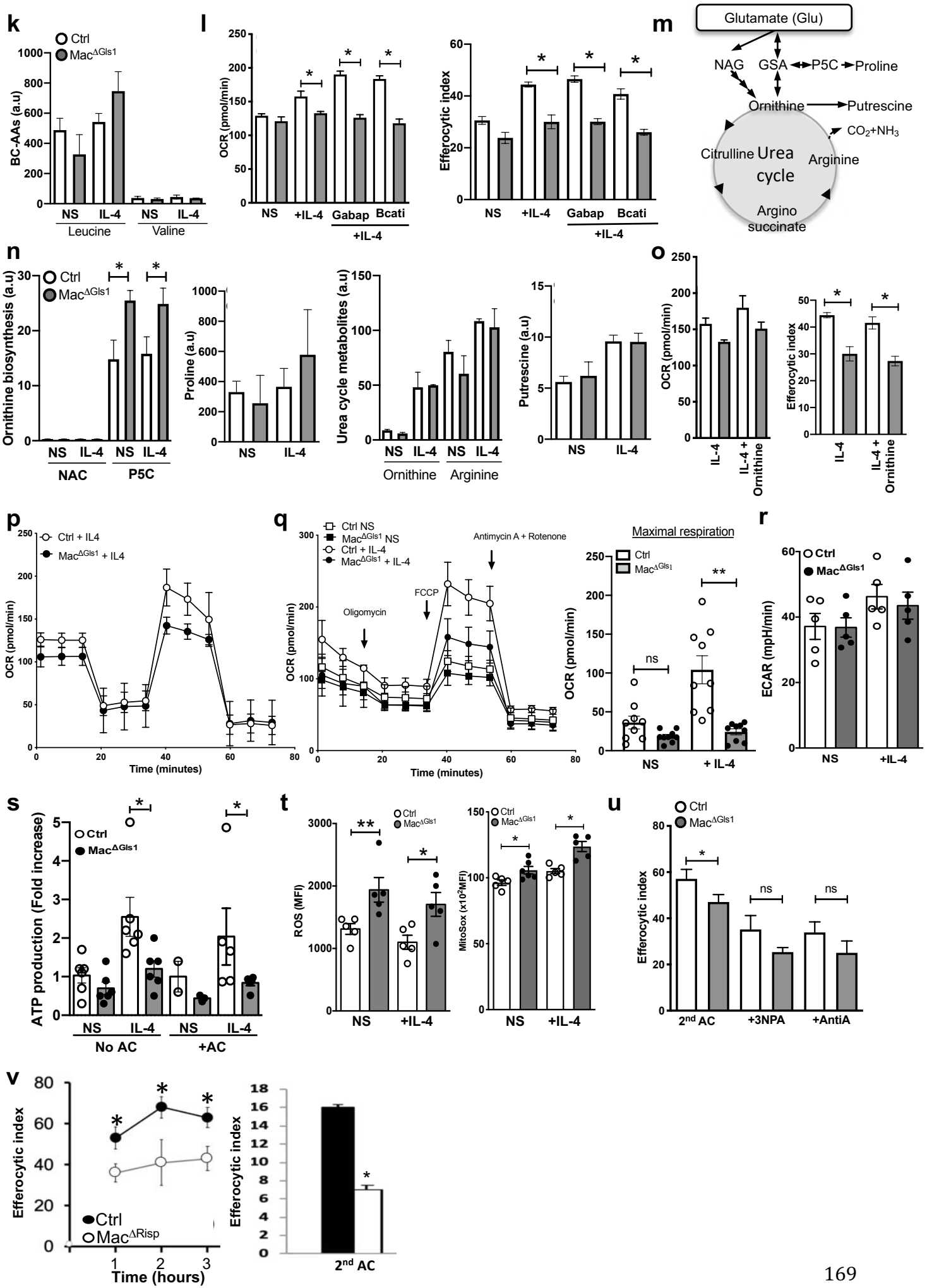
k
Ctrl
Mac^ΔGls1
BC-AAs (a.u)
NS
IL-4
Leucine
Valine
l
OCR (pmol/min)
Efferocytic index
NS
+IL-4
Gabap
Bcati
m
Glutamate (Glu)
NAG
GSA
P5C
Proline
Ornithine
Putrescine
CO2+NH3
Citrulline
Urea cycle
Arginine
Argino succinate
n
Ornithine biosynthesis (a.u)
NAC
P5C
Proline (a.u)
Urea cycle metabolites (a.u)
Ornithine
Arginine
Putrescine (a.u)
o
IL-4
IL-4 + Ornithine
p
Ctrl + IL4
Mac^ΔGls1 + IL4
Time (minutes)
q
Ctrl NS
Mac^ΔGls1 NS
Ctrl + IL-4
Mac^ΔGls1 + IL-4
Oligomycin
FCCP
Antimycin A + Rotenone
Maximal respiration
ns
r
ECAR (mpH/min)
s
ATP production (Fold increase)
No AC
+AC
t
ROS (MFI)
MitoSox (x10^4MFI)
u
2nd AC
+3NPA
+AntiA
v
Efferocytic index
Ctrl
Mac^ΔRisp
Time (hours)
2nd AC

Figure S3: Gls1-deficient macrophages have a defect in ATP-dependent corpse engulfment. (a) Schematic representation of efferocytosis steps and RNAseq analysis of "find-me", "eat-me" and "tolerate-me" signals in control and $Mac^{\Delta Gls1}$ PCMs stimulated overnight with IL-4. **(b)** Efferocytic index in control or $Mac^{\Delta Gls1}$ BMDMs stimulated overnight with IL-4 and incubated with either control or $Mac^{\Delta Gls1}$ media during the 45min efferocytosis. **(c)** Beads phagocytosis gating strategy (left) and quantification (right) in control or $Mac^{\Delta Gls1}$ BMDMs stimulated overnight with IL-4 and cultured with either basal or ACs media during the 45min efferocytosis. **(d)** Glutamine uptake in control or $Mac^{\Delta Gls1}$ BMDMs after [^{14}C]-Glutamine exposure. **(e)** Efferocytic index in control or $Mac^{\Delta Gls1}$ BMDMs in either basal condition, overnight IL-4 stimulation, and after a 4-hour glucose or glutamine deprivation. **(f)** Publicly available gene expression datasets analysis of macrophages ingesting apoptotic cells (GSE98169). **(g)** Gls1 mRNA expression and **(h)** Glutamine/Glutamate ratio during efferocytosis in control BMDMs in a time course experiment. **(i)** Clearance of fluorescent apoptotic debris 30min and 6 hours post-efferocytosis in control and $Mac^{\Delta Gls1}$ BMDMs. **(j)** Gating strategy and schematic representation of sealed and unsealed ACs. **(k)** Leucine and Valine levels by liquid chromatography-mass spectrometry in control or $Mac^{\Delta Gls1}$ BMDMs at steady state or after overnight IL-4 stimulation. **(l)** OCR and **(e)** efferocytic index in control or $Mac^{\Delta Gls1}$ BMDMs in basal conditions or stimulated overnight with IL-4 and +/- Gabapentin or Bcat inhibitor. **(m)** Schematic representation of glutamate utilization in the urea cycle. **(n)** Quantification of NAG, P5C, proline, ornithine, arginine and putrescine levels by liquid chromatography-mass spectrometry in control or $Mac^{\Delta Gls1}$ BMDMs in basal condition or following overnight IL-4 treatment. **(o)** OCR quantification (left) and efferocytic index (right) of control or $Mac^{\Delta Gls1}$ BMDMs treated overnight with IL-4 and ornithine. **(p)** OCR measured by Seahorse in control and $Mac^{\Delta Gls1}$ PCMs **(q)** OCR (left) and maximal respiration quantification (left) measured by Seahorse on control or $Mac^{\Delta Gls1}$ BMDMs with or without IL-4 stimulation. **(r)** ECAR measured by Seahorse in control or $Mac^{\Delta Gls1}$ BMDMs with or without overnight IL-4 stimulation. **(s)** ATP production measured by Seahorse in control or $Mac^{\Delta Gls1}$ BMDMs after one or no round of efferocytosis and +/- overnight IL-4 stimulation. **(t)** ROS (left) and Mitosox (right) quantification using flow cytometry in control or $Mac^{\Delta Gls1}$ BMDMs at steady state or following overnight IL-4 stimulation. **(u)** Efferocytic index in control or $Mac^{\Delta Gls1}$ BMDMs after either 2 rounds of efferocytosis or 3NPA +IL-4 or Antimycin A + IL-4 treatments overnight. **(v)** Efferocytic index after one round efferocytosis quantified by microscopy (left) or after two round efferocytosis measured by flow cytometry (right) in control or $Risp^{-/-}$ macrophages. All values are mean ± SEM and are representative of at least one experiment (n=3-9). **P*<0.05, ***P*<0.005 compared *to control*.

Figure S4

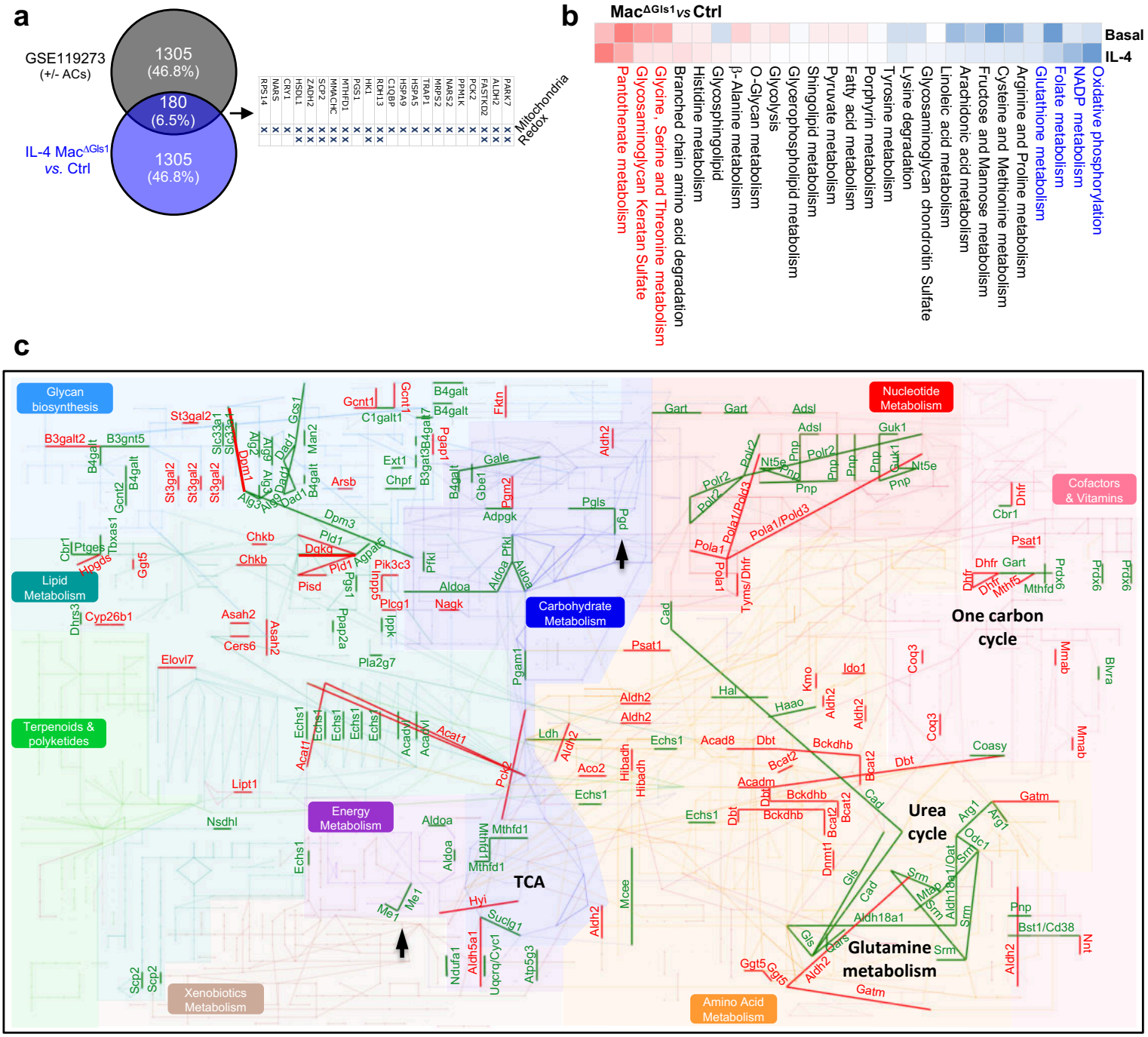
a
GSE119273
(+/- ACs)
1305
(46.8%)
180
(6.5%)
1305
(46.8%)
IL-4 Mac^ΔGls1
vs. Ctrl
RPS14 NARS CRY1 HSDL1 ZADH2 SCP2 MMACHC MTHFD1 PGS1 HK1 C1QBP RDH13 HSPA9 HSPA5 TRAP1 MRPS2 NARS2 PPM1K PCK2 FASTKD2 ALDH2 PARK7
Mitochondria Redox
b
Mac^ΔGls1 vs Ctrl
Basal
IL-4
Oxidative phosphorylation
NADP metabolism
Folate metabolism
Glutathione metabolism
Arginine and Proline metabolism
Cysteine and Methionine metabolism
Fructose and Mannose metabolism
Arachidonic acid metabolism
Linoleic acid metabolism
Glycosaminoglycan chondroitin Sulfate
Lysine degradation
Tyrosine metabolism
Porphyrin metabolism
Fatty acid metabolism
Pyruvate metabolism
Shingolipid metabolism
Glycerophospholipid metabolism
Glycolysis
O-Glycan metabolism
β-Alanine metabolism
Glycosphingolipid
Histidine metabolism
Branched chain amino acid degradation
Glycine , Serine and Threonine metabolism
Glycosaminoglycan Keratan Sulfate
Pantothenate metabolism
c
Glycan biosynthesis
Lipid Metabolism
Terpenoids & polyketides
Xenobiotics Metabolism
Energy Metabolism
Carbohydrate Metabolism
Nucleotide Metabolism
Cofactors & Vitamins
One carbon cycle
Urea cycle
Glutamine metabolism
TCA
Amino Acid Metabolism
d
GSH/GSSG ratio
Total glutathione (μM)
NADPH/NADP ratio
Ctrl
Mac^ΔGls1
NS
+IL-4
IL-4

Figure S4

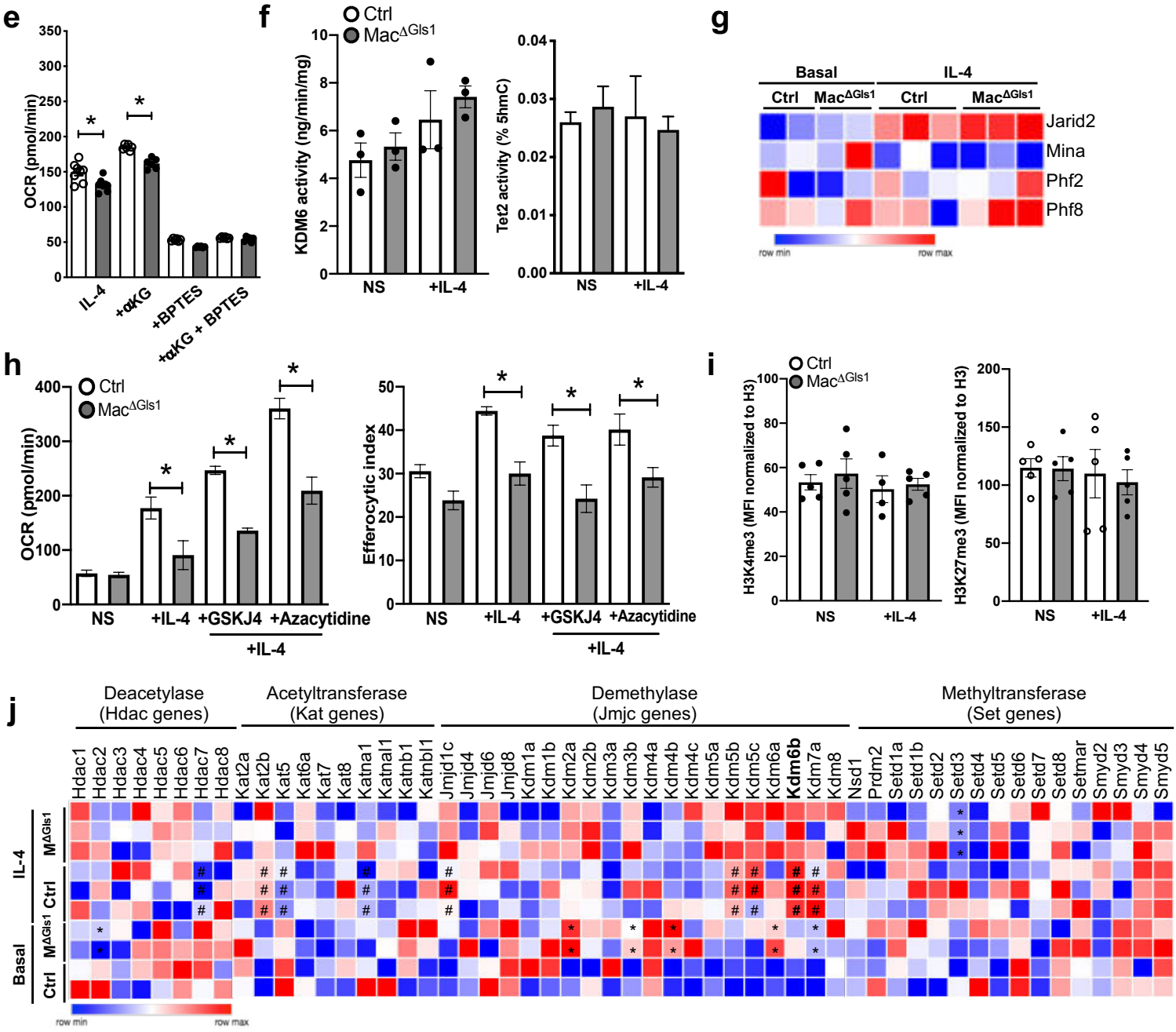
e
OCR (pmol/min)
IL-4
+αKG
+BPTES
+αKG + BPTES
f
Ctrl
MacΔGls1
KDM6 activity (ng/min/mg)
Tet2 activity (% 5hmC)
NS
+IL-4
g
Basal
IL-4
Ctrl
MacΔGls1
Jarid2
Mina
Phf2
Phf8
row min
row max
h
OCR (pmol/min)
Efferocytic index
NS
+IL-4
+GSKJ4
+Azacytidine
i
H3K4me3 (MFI normalized to H3)
H3K27me3 (MFI normalized to H3)
j
Deacetylase (Hdac genes)
Acetyltransferase (Kat genes)
Demethylase (Jmjc genes)
Methyltransferase (Set genes)
Hdac1 Hdac2 Hdac3 Hdac4 Hdac5 Hdac6 Hdac7 Hdac8
Kat2a Kat2b Kat5 Kat6a Kat7 Kat8 Katna1 Katnal1 Katnb1 Katnbl1
Jmjd1c Jmjd4 Jmjd6 Jmjd8 Kdm1a Kdm1b Kdm2a Kdm2b Kdm3a Kdm3b Kdm4a Kdm4b Kdm4c Kdm5a Kdm5b Kdm5c Kdm6a Kdm6b Kdm7a Kdm8
Nsd1 Prdm2 Setd1a Setd1b Setd2 Setd3 Setd4 Setd5 Setd6 Setd7 Setd8 Setmar Smyd2 Smyd3 Smyd4 Smyd5
IL-4
Basal
MΔGls1
Ctrl
row min
row max

Figure S4: GLS1 is essential for macrophage mitochondrial oxidative phosphorylation and redox balance but not epigenetic reprogramming. (a) Venn diagram from publicly available gene datasets (GSE119273). **(b)** Pathway enrichment analysis of RNA-seq profiling in control or $Mac^{\Delta Gls1}$ PCMs in basal conditions or stimulated overnight with IL-4. **(c)** KEGG mapping with DreamBio from RNAseq data of alternatively activated Gls1-deficient or sufficient PCMs. **(d)** GSH/GSSG ratio (left) and total glutathione concentration (middle) in control or $Mac^{\Delta Gls1}$ BMDMs at steady state and NADPH/NADP ratio (right) analyzed by liquid chromatography-mass spectrometry in control or $Mac^{\Delta Gls1}$ BMDMs at steady state or after overnight IL-4 stimulation. **(e)** OCR quantification in control or $Mac^{\Delta Gls1}$ BMDMs stimulated overnight with IL-4 and either □Ketoglutarate, BPTES, or □Ketoglutarate + BPTES. **(f)** KDM6 activity assay (left) and Tet2 activity assay (right) in control or $Mac^{\Delta Gls1}$ BMDMs in basal conditions or stimulated overnight with IL-4. **(g)** RNAseq analysis with focus on KDM6 target genes in control or $Mac^{\Delta Gls1}$ PCMs at steady state or after an overnight stimulation with IL-4. **(h)** OCR quantification (left) and efferocytic index (right) in control or $Mac^{\Delta Gls1}$ BMDMs in basal conditions or after an overnight stimulation with IL-4 and either GSKJ4 or azacytidine. **(i)** Global histone trimethylation modification assessed by flow cytometry using H3K4me3 and H3K27me3 staining in control and $Mac^{\Delta Gls1}$ BMDMs at steady state or stimulated overnight with IL-4. **(j)** RNAseq analysis with focus on epigenetic genes in control or $Mac^{\Delta Gls1}$ PCMs ($M^{\Delta Gls1}$) at steady state or after an overnight stimulation with IL-4. All values are mean ± SEM and are representative of at least one experiment (n=3-8). **P*<0.05 compared *to control*.

Figure S5

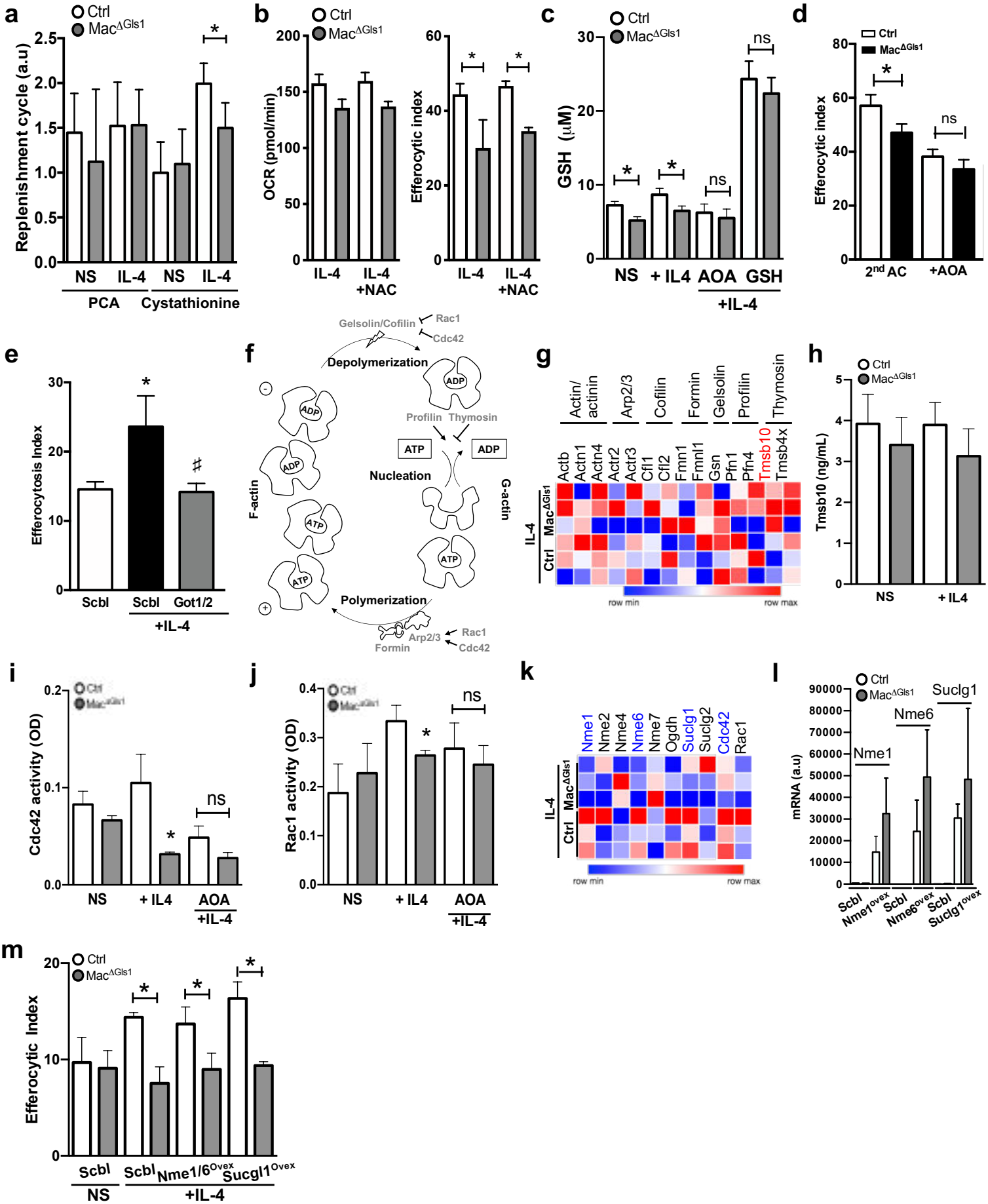
a
Ctrl
Mac^ΔGls1
Replenishment cycle (a.u)
NS
IL-4
NS
IL-4
PCA
Cystathionine
b
OCR (pmol/min)
Efferocytic index
IL-4
IL-4 +NAC
c
GSH (μM)
NS
+ IL4
AOA
GSH
+IL-4
d
Efferocytic index
2nd AC
+AOA
e
Efferocytosis Index
Scbl
Scbl
Got1/2
+IL-4
f
Gelsolin/Cofilin
Rac1
Cdc42
Depolymerization
Profilin
Thymosin
ATP
ADP
Nucleation
F-actin
G-actin
Polymerization
Arp2/3
Formin
g
Actin/ actinin
Arp2/3
Cofilin
Formin
Gelsolin
Profilin
Thymosin
Actb
Actn1
Actn4
Actr2
Actr3
Cfl1
Cfl2
Fmn1
Fmnl1
Gsn
Pfn1
Pfn4
Tmsb10
Tmsb4x
IL-4
Mac^ΔGls1
Ctrl
row min
row max
h
Tmsb10 (ng/mL)
NS
+ IL4
i
Cdc42 activity (OD)
NS
+ IL4
AOA
+IL-4
j
Rac1 activity (OD)
NS
+ IL4
AOA
+IL-4
k
Nme1
Nme2
Nme4
Nme6
Nme7
Ogdh
Suclg1
Suclg2
Cdc42
Rac1
IL-4
Mac^ΔGls1
Ctrl
row min
row max
l
mRNA (a.u)
Nme1
Nme6
Suclg1
Scbl
Nme1^ovex
Scbl
Nme6^ovex
Scbl
Suclg1^ovex
m
Efferocytic Index
Scbl
Scbl
Nme1/6^Ovex
Sucgl1^Ovex
NS
+IL-4

Figure S5: Non-canonical transaminase pathway is essential for actin dynamics and efferocytosis. (a) Effect of Gls1 deficiency on glutathione precursors (PCA, pyroglutamate; cystathionine) as a read out of cellular GSH replenishment. **(b)** OCR quantification (left) and efferocytic index (right) in control or $Mac^{\Delta Gls1}$ BMDMs treated overnight with IL-4 and IL-4 + N-Acetylcysteine (NAC). **(c)** GSH concentration in control or $Mac^{\Delta Gls1}$ BMDMs at steady state or treated overnight with IL-4 and either AOA or GSH. **(d)** Efferocytic index in control or $Mac^{\Delta Gls1}$ BMDMs after either 2 rounds of efferocytosis or AOA + IL-4 overnight treatment. **(e)** Efferocytic index in control or $Mac^{\Delta Gls1}$ BMDMs stimulated overnight or not with IL-4 and transfected with a scramble, or Got1/Got2 siRNA. **(f)** Schematic representation of actin polymerization and depolarization. **(g)** RNAseq analysis with focus on F-actin dynamic regulators in control or $Mac^{\Delta Gls1}$ PCMs stimulated overnight with IL-4. **(h)** Thymosin beta-10 concentration in control or $Mac^{\Delta Gls1}$ BMDMs in basal condition or stimulated overnight with IL-4. **(i)** Cdc42 activity and **(j)** Rac1 activity assay in control or $Mac^{\Delta Gls1}$ BMDMs in basal condition or stimulated overnight with IL-4 +/- AOA. **(k)** RNAseq analysis of ATP-GTP-converting enzymes in control or $Mac^{\Delta Gls1}$ PCMs stimulated overnight with IL-4. **(l)** qPCR quantification and **(m)** efferocytic index of Nme1, Nme6 and Suclg1 lentivirus overexpression in control or $Mac^{\Delta Gls1}$ BMDMs stimulated overnight with IL-4. All values are mean ± SEM and are representative of at least one experiment (n=3-6). **P*<0.05 compared *to control*.

Material and Methods

KEY RESOURCES TABLE

REAGENT or RESOURCE	SOURCE	IDENTIFIER
Antibodies		
Anti-α-actine HRP	Santa Cruz	sc-32251HRP RRID:AB_262054
Anti-CD68 (clone FA-11)	Bio-Rad	MCA1957 RRID:AB_322219
Anti-Glud1	Abcam	ab166618 RRID:AB_2815030.
Anti-Glutaminase	Abcam	ab93434 RRID:AB_10561964
Anti-IL-4 (clone 11B11)	BioXcell	BE0045 RRID:AB_1107707
Anti-Ki67 PE (clone 16A8)	Biolegend	652403 RRID:AB_2561524
Anti-Rat Alexa Fluor 488	ThermoFisher	A-11006 RRID:AB_2534074
c-Myc PE (Clone D84C12)	Cell Signaling	14819S RRID:AB_2798629
CD115 PE (clone AFS98)	eBioscience	12-1152-82 RRID:AB_465808
CD11b Brilliant Violet 510 (cloneM1/70)	Biolegend	101263 RRID:AB_2629529
CD11c APC (clone N418)	BD Biosciences	117309 RRID:AB_313778
CD206 PerCp-Cy5.5 (clone C068C2)	Biolegend	141715 RRID:AB_2561991
CD301 FITC (clone ER-MP23)	Bio-Rad	MCA2392 RRID:AB_872014
CD45 APC-Cy7 (clone 30-F11)	BD Biosciences	557659 RRID:AB_396774
CD64 Brillant Violet 421 (clone X54-5/7.1)	Biolegend	139309 RRID:AB_2562694
F4/80 PE-Cy7 (clone BM8)	Biolegend	123114 RRID:AB_893478
Histone H3 Alexa fluor 647 (clone D1H2)	Cell Signaling	12230S RRID:AB_2797852
ICAM-2 alexa fluor 647 (clone 3C4(MIC2/4))	Biolegend	105612 RRID:AB_2658040
MerTK PE (clone 2B10C42)	Biolegend	151506 RRID:AB_2617037
PD-L2 APC (clone B7-DC)	Biolegend	107210 RRID:AB_2566345
Phalloidine Alexa Fuor 594	InVitrogen	A12381 RRID:AB_2315633
Phospho-S6 Ribosomal Protein (ser235/236) PE (clone D57.2.2E)	Cell Signaling	5316S RRID:AB_10694989
Tri-Methyl-Histone H3 Lys27 Alexa fluor 647 (clone C36B11)	Cell Signaling	12158S RRID:AB_2797834+ E:F
Tri-Methyl-Histone H3 Lys4 Alexa fluor 647 (clone C42D8)	Cell Signaling	12064S RRID:AB_2797813
Chemicals, Peptides, and Recombinant Proteins		
^{13}C glutamine	Sigma	605166
^{14}C glutamine	PerkinElmer	NEC451050UC

^{3}H thymidine	PerkinElmer	NET027E250UC
3NPA	Sigma	164603
aKG	Sigma	349631
Annexin V PE	Biolegend	640908
Antimycin	Sigma	A8674
AOA	Sigma	C13408
Aspartate	Sigma	MAK095
Azacytidine	Sigma	A2385
BCAT inhibitor	Cayman Chemical	9002002
Bovine serum Albumin (BSA)	Sigma	A7030
BPTES	Sigma	SML0601
Cell Trace Violet proliferation kit	ThermoFisher	C34557
CFSE	ThermoFisher	C34570
Collagenase D	Sigma	11088882001
DAPI	Sigma	D9542
Substrate HRP	Sigma	WBKLS0500
EGCG	Sigma	E4143
Eosin	DiaPath	C0363
FCCP	Sigma	C2920
Fetal bovine serum	Fisher Scientific	12350273
Gabapentin	Sigma	G154
GSH	Sigma	G4251
GSK-J4	Sigma	SML0701
HBSS	Fisher Scientific	14175053
Hematoxylin Solution	Sigma	HHS32
High-Capacity cDNA reverse transcription kit	Applied Biosystems	4368814
IL-4	Peprotech	200-04
L-Glutamine	ThermoFisher	25030024
L-ornithine	Sigma	75440
Lipofectamine RNAiMAX	Fisher Scientific	13778150
Lysing buffer	BD Biosciences	555899
M-CSF	Miltenyi	130-101-704
Mitoquinol	Cayman Chemical	89950
MitoSOX Red	Thermofisher	M36008
Mouse Foxp3 Buffer Set	Biosciences	560409
NAC	Sigma	A7250
OCT	TEK	4583-01
Oil Red O	Sigma	O0625
Oligomycin	Sigma	75351
PBS 1X	Fisher Scientific	14190169
Penicillin-Streptomycin	Fisher Scientific	15140130
Percoll	Sigma	P1644
PFA 4%	VWR International	9713.1000
Poly-I:C	Invivogen	TLRL-PIC-5
Protease inhibitor cocktail	Sigma	P8340
RIPA buffer	Cell signaling	9806
RNeasy Plus Mini Kit (250)	QIAGEN	74136
ROS	Thermofisher	C6827

Rotenone	Sigma	R8875
RPMI medium	Fisher Scientific	31870074
Tempol	Sigma	581500
Critical Commercial Assays		
DNA Hydroxymethylation (5-hmC) ELISA	Euromedex	P-1032-96
Glutamine/Glutamate-Glo™ Assay	Promega	J8022
GSH/GSSG-Glo™ Assay	Promega	V6611
KDM6A/ KDM6B Activity	Abcam	ab156910
LabAssay(TM) Cholesterol	Sobioda	W1W294-65801
Rac1 G-LISA	Euromedex	CS-BK128
Triglycerides assay	Diasys	1 5710 99 10021
TUNEL Assay Kit - FITC	Abcam	ab66108
Deposited Data		
RNAseq	NCBI GEO	GEO: GSE to complete
Experimental Models: Organisms/Strains		
Mouse: ApoE KO	Jackson Laboratory	002052 RRID:IMSR_JAX:002052
Mouse: Gls1fl/fl	Pr. Stephen Rayport's lab	N.A.
Mouse: Glud1fl/fl	Pr. Pierre Maechler's lab	N.A.
Mouse: LyzM^{cre}	Jackson Laboratory	004781 RRID:IMSR_JAX:004781
Mouse: Mx1^{cre}	Jackson Laboratory	003556 RRID:IMSR_JAX:003556
Oligonucleotides		
Got1 siRNA	Dharmacon	L-043492-01-0010
Got2 siRNA	Dharmacon	L-043495-01-0010
Scramble siRNA	Dharmacon	D-001810-01-05
Software and Algorithms		
FlowJo	Tree Star	N.A.
ImageJ	NIH	N.A.
Phantasus	http://genome.ifmo.ru/phantasus/	N.A.
Prism8	GraphPad	N.A.
StepOne Software v.2.2.2	Applied Biosystem	N.A.
Other		
Western Diet	Ssniff	TD88137

Human atherosclerosis. Tissue collection was part of the Maastricht Pathology Tissue Collection (MPTC) and further storage and use of the tissue was in line with the Dutch Code for Proper Secondary use of Human Tissue and the local Medical Ethical Committee (protocol number 16-4-181).
Carotid arteries were collected from symptomatic patients undergoing carotid endarterectomy (CEA). Formalin-fixed, paraffin embedded (FFPE) 5mm-segments were alternated with frozen segments for RNA isolation. FFPE segments were then classified as fibrous cap atheroma with or without intraplaque hemorrhage (stable or unstable respectively) according to haematoxylin-eosin (HE) staining.1 Forty-four paired stable and unstable snap-frozen

segments from 22 symptomatic patients undergoing CEA in the Maastricht human plaque study (MaasHPS) were only used for further microarray analysis when both adjacent plaque segments showed the same histological classification. Snap-frozen segments were pulverized and 5-20mg of material was subjected for transcriptomics. RNA isolation was performed by Guanidium Thiocyanate extraction and further purified with the Nucleospin RNA II kit (Macherey-Nagel GmbH&Co). RNA quality and integrity were determined using the Agilent 2100 Bioanalyzer. Biotinylated cRNA was prepared with Illumina TotalPrep RNA Amplification Kit (Ambion, TX, U.S.A) and 750ng cRNA per sample was used for hybridization (Illumina Human Sentrix-8 V2.0, Beadchip®). Scanning was performed on the Illumina Beadstation 500 (Illumina, CA, U.S.A) and image analysis was done using the Illumina Beadstudio v3 Gene expression software. A total of 22,184 human transcripts were analyzed in R Bioconductor lumi package.2 Firstly, a variance stabilizing transformation, which is incorporated in the lumi package, was performed. Secondly, Robust Spline Normalization (RSN) algorithm in lumi package was applied to normalize the data. Differential gene expression analysis was done by using the function lmFit() provided in Limma R package on preprocessed transcriptomics data.3
The 88 adjacent tissue sections were phenotyped extensively for plaque size, necrosis, inflammation (CD68, CD3, arginase, iNOS), SMCs (αSMA), collagen (Sirius red) and angiogenesis (CD31+ microvessel density, newly formed CD105+ microvessels, αSMA+ mature microvessels, Lyve+ lymphatic density). Pearson correlation analysis was performed to assess the association between gene expression and plaque phenotypical traits.

Mice. Gls1$^{fl/fl}$ mice were kindly provided by Pr. Stephen Rayport and have been crossed to Lyz2^{Cre} mice (B6.129P2-Lyz2tm1(cre)Ifo/J, The Jackson Laboratory) or Mx1^{cre} mice (B6.Cg-Tg(Mx1-cre)1Cgn/J) and brought on ApoE-deficient genetic background (B6.129P2-ApoEtm1Unc/J). Mx1^{cre} mice (B6.Cg-Tg(Mx1-cre)1Cgn/J) were also crossed to Glud1 floxed mice (kindly provided by Pr. Pierre Maechler). For each experiment, co-housed littermate controls were used. Animal protocols were approved by the Institutional Animal Care and Use Committee of the French Ministry of Higher Education and Research and the Mediterranean Center of Molecular Medicine (Inserm U1065) and were undertaken in accordance with the European Guidelines for Care and Use of Experimental Animals. Animals had free access to food and water and were housed in a controlled environment with a 12-hour light–dark cycle and constant temperature (22°C). Hyperlipidemia was induced by feeding the mice with a Western diet (TD88137, Ssniff) for 12 weeks. Mice were weighted every two weeks following Western diet induction.

Poly(I:C) induction. Mx1^{cre} mice were i.p. injected with 1mg/mL poly(I:C) three times every two days(Kuhn et al., 1995). Mice were then used for experimentation 3 weeks later.

IL-4c in vivo treatment. Mice were i.p. injected with IL-4 complexed to anti-IL-4 mAb (IL-4c; containing 5 µg of IL-4, PeproTech, and 25 µg of anti-IL-4 clone 11B11, BioXcell). 36 hours later, PCMs were collected and analyzed by flow cytometry.

Cell culture, LPMs and BMDMs generation. BM cells were harvested from mouse femur and tibia and differentiated in the presence of recombinant mouse M-CSF (20 ng/ml; Miltenyi) in complete RPMI 1640 medium (Corning) containing 10mM glucose, 2mM L-glutamine, 100U/ml of penicillin/streptomycin, and 10% FBS for 7 days at 37°C and 5% CO2.

Cell treatments. At day 7 BMDMs were collected, plated and activated overnight as indicated. Peritoneal cells were obtained by peritoneal lavage with 5ml of PBS. Cells were plated and cultured overnight in complete RPMI 1640 medium (Corning) containing 10mM glucose, 2mM L-glutamine, 100U/ml penicillin/streptomycin, and 10% FBS at 37°C and 5% CO2. Cell were incubated overnight with the following treatments: IL-4 (20ng/mL, Peprotech), AOA (200µM, Sigma), Dimethyl-α-ketoglutarate (1mM, Sigma), EGCG (100µM, Sigma), GSH (10mM, Sigma), BPTES (10µM, Sigma), L-ornithine (1mM, Sigma), BCATc inhibitor (20µM, Cayman

Chemical), Gabapentin (10µg/mL, Sigma), GSKJ4 (20µM, Sigma), Azacytidine (100µM, Sigma), 3NPA (1.68mM, Sigma), Antimycin A (0.1µM, Sigma), Tempol (4mM, EMD Millipore), mitoquinol (200nM, Cayman Chemical), NAC (10mM, Sigma), Aspartate (5µg/mL, Sigma). For glutamine and glucose deprivation, glucose or glutamine free media were used, and cells were deprived for 4 hours before the experiments.

siRNA transfection. Cells were transfected with Got1/Got2 siRNA (L-043492-01-0005 and L-043495-01-0005, Dharmacon) or control siRNA (D-001810-01-05, Dharmacon) (referred to as Scbl) at 30 nM using Lipofectamine RNAiMAX (Life Technologies), according to the manufacturer's instructions.

Lentivirus overexpression. Cells were spin-transfected for 90min at 2500 rpm with Gls1, Nme1/Nme6 or suclg1 lentivirus (LVM(VB200119-1197bpk)-C, LVM(VB200120-1064ucb)-C, LVM(VB200120-1213tjc)-C, LVM(VB200120-1214hxx)-C respectively, Vectorbuilder) or control lentivirus (LVM(VB200120-1215tyv)-C, Vectorbuilder) (referred to as Scbl) and used at MOI 10. After 6 hours, cells were washed, and the media replaced with fresh media.

Western Blotting. LPMs were cell-sorted and then lysed in RIPA buffer containing protease inhibitors cocktail (ThermoFisher) and agitated for 1 hour at 4°C before centrifugation at 14000 rpm for 10min at 4°C. Supernatants were sampled and later used for SDS-PAGE. Protein content was evaluated using Pierce™ BCA assay kit (ThermoFisher). Protein samples were resolved on 10% SDS-PAGE gels and were then transferred onto polyvinylidene difluoride membrane using a wet transfer system. Membranes were blocked in 5% (w/v) BSA in Tris-buffered saline-Tween for one hour at room temperature. Membranes were then incubated with primary antibody (anti-Glud1 or anti-Gls1 antibodies (Abcam)) followed by the appropriate horseradish peroxidase-conjugated secondary antibody. Anti α-actin mAb (Santa Cruz) was used as loading control. Proteins were detected by substrate HRP (Sigma).

Analysis of atherosclerotic plaque. Mice were sacrificed and slowly perfused with 10ml of ice-cold PBS. The hearts and aortas were carefully excised and fixed in 4% paraformaldehyde containing 30% sucrose. The aortas were stained with Oil Red O (Sigma- O0625) to evaluate plaque neutral lipid content as previously described (Yun et al., 2017). The hearts were embedded in OCT compound (Gentaur) and stored at –80°C before analysis. 10µm cryosections of the aortic sinus were prepared. Oil Red O staining was used to detect neutral lipid content in the plaque combined with a haematoxylin/eosin staining to analyse tissue architecture. Plaque macrophages were visualized using purified anti-CD68 mAb (clone FA-11, AbD Serotec). Anti-rat Alexa Fluor 488-conjugated antibody (A-11006, Life technologies) was used for detection of CD68 staining. For analysis of plaque macrophage proliferation, anti-Ki67 PE conjugated mAb (clone 16A8, BioLegend) was used. Nuclei were revealed with DAPI counterstaining (2µg/ml). TUNEL staining was performed using the DeadEnd™ Fluorometric TUNEL System (Promega). Plaque area quantification were measured with ImageJ software.

Echography. Animals were fully anesthetized with 1.5% Isoflurane before and during ultrasound scanning. Before all ultrasound scanning, the hair of the mouse chest wall was carefully removed, and warm ultrasound transmission gel was liberally applied to ensure optimal image quality. Echocardiography was performed using a high-frequency Vevo2100 (Visualsonics)-imaging.

Transmission Electronic Microscopy. Cells were observed with transmission electron microscopy (TEM) for ultrastructural analysis. Cells were fixed in a 1.6 % glutataraldehyde solution in 0.1 M sodium phosphate buffer at room temperature (RT) and stored overnight at 4°C. After three rinsing in 0.1 M cacodylate buffer (15 min each), cells were postfixed in a 1 % osmium tetroxide and 1 % potassium ferrocyanide solution in 0.1 M cacodylate buffer for 1 hour at RT. Cells were subsequently dehydrated in a series of acetone baths (90 %, 100% three times, 15 min each) and progressively embedded in Epon 812 resin (acetone / resin 1:1,

100 % resin two times, 2 hours for each bath). Resin blocs were finally left to harden in a 60 °C oven for 2 days. Ultrathin sections (70 nm) were obtained with a Reichert Ultracut S ultramicrotome equipped with a Drukker International diamond knife and collected on 200 mesh copper grids. Sections were stained with lead citrate and uranyl acetate. TEM observations were performed with a JEOL JEM-1400 transmission electron microscope, equipped with a Morada camera, at a 100kV acceleration voltage.

In vitro efferocytosis analysis. BMDMs and PCMs were generated and stimulated as described above.
To generate apoptotic cells (ACs), thymii from C57BL/6J mice were harvested and mechanistically dissociated, filtered on 100µm nylons (Falcon), pelleted and resuspended in RPMI medium supplemented with 10% FBS. Apoptosis was induced by UV exposure at 312nm for 10min and cells were maintained in culture for an additional 2 hours. This method results in 70-90% apoptotis (Yvan-Charvet et al., 2010). ACs were labelled with CellTrace™ Violet Cell Proliferation kit (ThermoFisher) according to the manufacturer's instructions. Fluorescent ACs were washed twice with PBS before use.
For one round efferocytosis: Stained apoptotic cells (ACs) were added at a 5:1 ratio on plated macrophages for 45min.
For two rounds efferocytosis: Unlabelled apoptotic lymphocytes (ACs) were added at a 5:1 ratio on plated macrophages for 45min. Cells were then washed 3 times and macrophages were incubated for 1h. Stained apoptotic lymphocytes (ACs) were then added at a 5:1 ratio on macrophages for 45min.
Cells were washed 3 times and macrophages were stained and analysed for AC content and activation markers by flow cytometry. For Seahorse extracellular flux analysis ACs were injected directly, before drug treatment, during the assay.

Histology. BMDMs and ACs were generated and stimulated as described above. ACs were stained with CellTrace™ CFSE (Invitrogen) for 30min prior to one round efferocytosis. After 15min of efferocytosis, BMDMs were washed with a 37°C heated medium and fixed for 10min at 37°C with 4% paraformaldehyde culture medium. Cells were then saturated for 30min in PBS 10% FBS. Cells were incubated for 30min with Texas Red™-X Phalloidin (Invitrogen). Cells were then washed thoroughly, and coverslips were mounted with aqueous glue. Sections were observed the following day by fluorescent microscopy.

Find-me experiments. To test whether cells had a different ability to sense ACs we applied "taste-me" experiments. BMDMs were generated and stimulated as described above. Immediately before one-round efferocytosis, BMDMs culture medium was either left or inverted between the two genotypes. In the second experiment, immediately before one-round efferocytosis, BMDMs culture medium was either left or replaced by ACs culture medium.

In vivo efferocytosis analysis. ACs were generated as described above. Mice were i.v injected with $2*10^7$ stained ACs and 1 hour later, the spleen and liver were collected and analysed by flow cytometry.

In vitro flow cytometry analysis. Cells were stained for 25 min at 4°C protected from light. For flow cytometry analysis the following list of antibodies was used: MitoSOX™ Red (ThermoFisher), ROS (Thermofisher, CM-H2DCFDA), CD206 PerCp-Cy5.5 conjugated (clone C068C2, BioLegend), PD-L2 APC conjugated (Clone B7-DC, Biolegend), MerTK PE conjugated (clone 2B10C42, BioLegend), CD115 PE conjugated (clone AFS98, eBioscience), CD64 Brillant Violet 421 conjugated (clone X54-5/7.1, BioLegend), F4/80 Pe-Cy7 conjugated (clone BM8, BioLegend), Annexin V (Biolegend), CD4 FITC conjugated (Clone RM4.5), CD8b FITC conjugated (Clone YTS156.7.7). Cells were then washed, centrifuged and data were acquired on BDFACSCanto flow cytometer. Analysis was performed using FlowJo software (Tree Star).

Intracellular flow cytometry. For all intracellular stainings: Phospho-S6 Ribosomal Protein (Ser235/236) PE conjugated (clone D57.2.2E, Cell signaling), c-Myc PE Conjugate (Clone D84C12, Cell signaling), Tri-Methyl-Histone H3 (Lys27) Alexa Fluor® 647 Conjugated (Clone C36B11), Histone H3 (Alexa Fluor® 647 Conjugated (Clone D1H2), Tri-Methyl-Histone H3 (Lys4) Alexa Fluor® 647 conjugated (Clone C42D8), CD4 APC conjugated (Clone RM4.5), CD8b Alexa Fluor® 647 Conjugated (Clone YTS156.7.7). Cells were removed from media, stained for surface, fixed, then stained for intracellular proteins using Foxp3 Transcription Factor Fixation/Permeabilization kit (BD biosciences).

In vivo flow cytometry analysis. Cells were collected from spleen, peritoneal cavity, bone marrow, liver and brain. Splenocytes were extracted by pressing spleens through a stainless-steel grid. Peritoneal and bone marrow leukocytes were harvested by PBS lavage. Liver and brain were cut in small piece and digested for 30min with HBSS medium containing 1,5mg/mL collagenase D (Roche) at 37°C. For liver and microglia preparation, an additional purification step was performed by Percoll gradient. Single-cell suspension was submitted to red blood cell lysis, filtration and centrifugation for 5min at 1,500rpm. Cell suspensions were stained with the appropriate antibodies for 30min on ice protected from light. The following antibodies were used for macrophage flow cytometric analysis: CD11b Brillant Violet 510 conjugated (clone M1/70, BioLegend), CD115 PE conjugated (clone AFS98, eBioscience), CD45 APC-Cy7 conjugated (clone 30-F11, BD Biosciences), CD64 Brillant Violet 421 conjugated (clone X54-5/7.1, BioLegend), CD11c APC conjugated (clone N418, BioLegend), F4/80 Pe-Cy7 conjugated (clone BM8, BioLegend), CD206 PerCp-Cy5.5 conjugated (clone C068C2, BioLegend), CD301 FITC conjugated (clone ER-MP23, Bio-Rad). Cells were then washed, centrifuged and data were acquired on BDFACSCanto flow cytometer. Analysis was performed using FlowJo software (Tree Star).

Seahorse extracellular flux analysis. For extracellular flux assay, 1×10^5 BMDMs or LPMs were plated in a Seahorse Bioscience culture plate. Cells were then incubated overnight with different drugs and metabolites. OCR and ECAR was measured by an XF96 Seahorse Extracellular Flux Analyzer following the manufacturer's instruction. In the seahorse assay, cells were treated with oligomycin (1µM), FCCP (1.5µM), rotenone (1µM) and antimycin A (0.1µM). Each condition was performed in 3 replicates.

RNAseq. PCMs were obtained by lavage as described above. Then cells were stained with CD64 Brilliant Violet 421 conjugated (clone X54-5/7.1), ICAM-2 alexa fluor 647 conjugated (clone 3C4(MIC2/4)) and CD115 PE conjugated (clone AFS98). These antibodies allow us to separate the two subsets of peritoneal macrophages with only the major one expressing ICAM-2 (Gautier et al., 2012; Kim et al., 2016). Cells were cell sorted on BD FacsAria flow cytometer. Total RNA was extracted with RNeasy Mini Kit (Qiagen) according to the manufacturer's protocol and quality was assessed by Nanodrop (Ozyme). Library construction were conducted as described previously (Jha et al., 2015). Libraries were sequenced at the Centre for Applied Genomics (SickKids, Toronto) using a HiSeq 2500 (Illumina).

Integrated network analyses. Network-based integration of metabolite and gene expression datasets was conducted using Shiny Gam as previously described (Jha et al., 2015). We also developed *DreamBio*, a complementary topological tool for Integrated Network Analysis mapped into KEGG pathway. The same strategy than Shiny Gam was used by downloading KEGG REACTION, KEGG ENZYME, KEGG COMPOUND, and KEGG GLYCAN databases (August 2013 version) except that GEPHI GEXF (graph exchange format) was converted from KGML to be analyzed through Sigma library js dedicated to graph drawing. Up and down regulated metabolic genes based on p values calculated with Phantasus (Jha et al., 2015) were mapped into models maintaining all essential KEGG pathway attributes. DreamBio will become soon freely available at http://dreamsession.com/biotest/bioinfo/index.php?w=sigma.

Fluxomics. Metabolite extraction of BMDMs was performed on 2.5 million cells per well using 70°C aqueous 70% ethanol as described previously (Devos et al., 2019). At collection, cells were placed immediately on ice, the media was removed, and cells were washed three times with ice-cold PBS to remove residual media. Intracellular metabolites were extracted twice with hot ethanol. For LCMS, samples where dried under nitrogen flow and reconstituted in a milliQ water/acetonitrile (1:1) mixture for injection using a UPLC Acquity (Waters) separation system coupled with a Xevo G2 ToF (Waters). Compounds were ionized using an electrospray ionization source in negative mode. Data processing was performed in MATLAB (Mathworks, Inc.) using a custom-made in-house protocol. Compound identification was performed using both retention time of authentic standards and accurate mass with an accepted deviation of 0.005 Da. Raw data was converted to netCDF format using Chemstation (Agilent), before processing in MATLAB R2014b (Mathworks, Inc.) using PARADISe software. All MS sample processing and analysis were performed by MS-Omics, Inc. (Copenhagen, Denmark).

Metabolomics. Metabolomics analyses were performed at CriBioM as previously described (Aidoud et al., 2018). Briefly, control and Gls1-deficient BMDMs were treated with or without 20ng/mL IL-4 as indicated in the figure legends. Metabolites were extracted by exposing cells to cold methanol and analyzed by LC-MS.

Typhoon™ Biomolecular Imager. 2µCi of [^{14}C]-labelled glutamine were i.v. injected and mice were sacrificed 15 minutes later. Aortas were harvested and the associated adipose tissue was carefully dissected and removed. Imaging for [^{14}C]-labelled glutamine was performed on Typhoon™ Biomolecular Imager (Amersham). Whole mount staining with Oil Red O paralleled this analysis on the same samples.

Thin-Layer Chromatography (TLC). Aortic tissues were homogenized with 5% HClO4 solution and the radioactivity incorporated in this extract was measured before being dropped on silica-gel POLYGRAM precoated TLC sheets (Sigma). Separation of ^{14}C glutamine and the ^{14}C glutamine-derived glutamate was achieved in hexane/diethylether/formic acid (80:20:1 v/v/v) running buffer. The radioactivity was quantified and expressed as a percentage of ingested radioactivity.

[^{14}C]- Glutamine incorporation. BMDMs were generated and stimulated as described above. Four hours before the experiment, cells were deprived in glutamine or put in presence of medium containing 1mM glutamine. [^{14}C]-Glutamine (1µCi) was added on cells for 18 hours. Cells were collected, centrifuged, washed with PBS, and resuspended in NaOH (0.1N)/SDS (0,1%) before adding scintillation.

[^{3}H]-Thymidine incorporation. BMDMs were generated and stimulated as described above. The day before the experiment, cells were stimulated overnight with IL-4 (20ng/µL). [^{3}H]-Thymidine (1µCi) was added on cells in regular media for 2 hours. Cells were collected, centrifuged, washed with PBS, and resuspended in NaOH (0.1N)/SDS (0,1%) before adding scintillation.

Glutamine and glutamate measurement. To analyse macrophage glutamine and glutamate content we used a commercially available kit Glutamine/Glutamate-Glo™ Assay (Promega) in accordance with the manufacturer's instructions. Briefly, BMDMs and PCMs were incubated as previously described and washed three times with PBS to remove remaining cell culture medium. Cells were then subjected to osmotic lysis with DI water before following the manufacturer's instructions.

Plasma cholesterol and triglycerides content. Plasma cholesterol and triglyceride content was measured with LabAssayTM Cholesterol (Sobioda) and Triglycerides Reagent (Diasys) according to the manufacturer's protocol.

Intracellular GSH/GSSG assay. The reduced glutathione (GSH)/ oxidized glutathione (GSSG) balance was determined using GSH/GSSG-Glo™ Assay (Promega) according to the manufacturer's instructions.

Rac1 and Cdc42 activity assay. Rac1 and Cdc42 activities were determined with Rac1 G-LISA Activation Assay Kit (Cytoskeleton BK128) and Cdc42 G-LISA Activation Assay Kit (Cytoskeleton BK127) according to the manufacturer's instructions.

G-Actin/F-Actin assay. G-Actin/F-Actin activity was determined with G-Actin/F-Actin In Vivo Assay Biochem Kit (Cytoskeleton) according to the manufacturer's instructions.

Actin polymerization assay. Actin polarization activity was determined with Actin Polymerization Biochem Kit (Cytoskeleton) according to the manufacturer's instructions.

KDM6 activity assay. KDM6 activity was determined with KDM6A/ KDM6B Activity Quantification Assay Kit (Abcam) according to the manufacturer's instructions.

Tet2 activity assay. Tet2 activity was determined with MethylFlash Global DNA Hydroxymethylation (5-hmC) ELISA Easy Kit (Epigentek) according to the manufacturer's instructions.

Real-Time qPCR. Total RNA was isolated using the RNeasy Plus Mini kit (QIAGEN) and quantified using a Nanodrop (Ozyme). cDNA was prepared using 10 ng/µl total RNA by a RT-PCR using a high capacity cDNA reverse transcription kit (Applied Biosystems), according to the manufacturer's instructions. Real-time qPCR was performed on cDNA using SYBR Green. qPCRs were performed on StepOne device from Applied Biosystem (France). Samples were performed in triplicates. Results are expressed in arbitrary units. Gls1 (GCACATTATTCACCCGGTAACC; CTGCCCACCCACCATCC, Thermofisher)

Statistics. Data are expressed as mean+/- SEM. Statistical analysis was performed using a 2-tailed t test or ANOVA (with Tukey's post-test analysis) with GraphPad Prism software. A P value ≤ 0.05 was considered as statistically significant.

Acknowledgments. We thank Béatrice Caraveo for computional development of DreamBio, a novel topological tool for Integrated Network Analysis. We thank Samantha Fernandez for the non-invasive study of atheroma plaques by ultrasound echography as part of the European Center for Research in Imaging (Cerimed), Dr Fréderic Labret for assistance with flow cytometry, Dr Véronique Corcelle for assistance in animal facilities and Dr. Marie Irondelle for assistance with confocal microscopy.

Financial support and sponsorship. This work was supported by grants from the Fondation de France (FDF) and the European Research Council (ERC) consolidator program (ERC2016COG724838) to L.Y.C. CCMA electron microscopy equipments have been funded by the Région Sud - Provence-Alpes-Côte d'Azur, the Conseil Départemental des Alpes Maritimes, and the GIS-IBiSA

Conflict of interest: The authors have declared that no conflict of interest exists.

References

A-Gonzalez, N., Bensinger, S.J., Hong, C., Beceiro, S., Bradley, M.N., Zelcer, N., Deniz, J., Ramirez, C., Díaz, M., Gallardo, G., de Galarreta, C.R., Salazar, J., Lopez, F., Edwards, P., Parks, J., Andujar, M., Tontonoz, P., Castrillo, A. Apoptotic cells promote their own clearance and immune tolerance through activation of the nuclear receptor LXR. Immunity. 2009 Aug 21;31(2):245-58.

Aidoud, N., Delplanque, B., Baudry, C., Garcia, C., Moyon, A., Balasse, L., Guillet, B., Antona, C., Darmaun, D., Fraser, K., et al. (2018). A combination of lipidomics, MS imaging, and PET scan imaging reveals differences in cerebral activity in rat pups according to the lipid quality of infant formulas. FASEB J *32*, 4776-4790.

Aspenström, P. (2004). Integration of signalling pathways regulated by small GTPases and calcium. Biochim Biophys Acta *1742*, 51-8.

Bauer, T.M., Murphy, E. (2020). Role of Mitochondrial Calcium and the Permeability Transition Pore in Regulating Cell Death. Circ Res *126*, 280-293.

Boissan M, Schlattner U, Lacombe ML. The NDPK/NME superfamily: state of the art. Lab Invest. 2018 Feb;98(2):164-174.

Bosurgi, L., Cao, Y.G., Cabeza-Cabrerizo, M., Tucci, A., Hughes, L.D., Kong, Y., Weinstein, J.S., Licona-Limon, P., Schmid, E.T., Pelorosso, F., et al. (2017). Macrophage function in tissue repair and remodeling requires IL-4 or IL-13 with apoptotic cells. Science *356*, 1072-1076.

Caron, E., Hall, A. (1998). Identification of two distinct mechanisms of phagocytosis controlled by different Rho GTPases. Science *282*, 1717-21.

Chandel, N.S. (2015). Evolution of Mitochondria as Signaling Organelles. Cell Metab *22*, 204-206.

DeBerardinis, R.J., and Cheng, T. (2010). Q's next: the diverse functions of glutamine in metabolism, cell biology and cancer. Oncogene *29*, 313-324.

Devos, M., Mogilenko, D.A., Fleury, S., Gilbert, B., Becquart, C., Quemener, S., Dehondt, H., Tougaard, P., Staels, B., Bachert, C., et al. (2019). Keratinocyte Expression of A20/TNFAIP3 Controls Skin Inflammation Associated with Atopic Dermatitis and Psoriasis. J Invest Dermatol *139*, 135-145.

Dixon, S.J., Lemberg, K.M., Lamprecht, M.R., Skouta, R., Zaitsev, E.M., Gleason, C.E., Patel, D.N., Bauer, A.J., Cantley, A.M., Yang, W.S., et al. (2012). Ferroptosis: an iron-dependent form of nonapoptotic cell death. Cell *149*, 1060-1072.

Elliott, M.R., and Ravichandran, K.S. (2016). The Dynamics of Apoptotic Cell Clearance. Dev Cell *38*, 147-160.

Fan, J., Ye, J., Kamphorst, J.J., Shlomi, T., Thompson, C.B., and Rabinowitz, J.D. (2014). Quantitative flux analysis reveals folate-dependent NADPH production. Nature *510*, 298-302.

Gautier, E.L., Shay, T., Miller, J., Greter, M., Jakubzick, C., Ivanov, S., Helft, J., Chow, A., Elpek, K.G., Gordonov, S., et al. (2012). Gene-expression profiles and transcriptional regulatory pathways that underlie the identity and diversity of mouse tissue macrophages. Nat Immunol *13*, 1118-1128.

Grabner, R., Lotzer, K., Dopping, S., Hildner, M., Radke, D., Beer, M., Spanbroek, R., Lippert, B., Reardon, C.A., Getz, G.S., et al. (2009). Lymphotoxin beta receptor signaling promotes tertiary lymphoid organogenesis in the aorta adventitia of aged ApoE-/- mice. J Exp Med *206*, 233-248.

Han, C.Z., and Ravichandran, K.S. (2011). Metabolic connections during apoptotic cell engulfment. Cell *147*, 1442-1445.

Jais, A., Einwallner, E., Sharif, O., Gossens, K., Lu, T.T., Soyal, S.M., Medgyesi, D., Neureiter, D., Paier-Pourani, J., Dalgaard, K., et al. (2014). Heme oxygenase-1 drives metaflammation and insulin resistance in mouse and man. Cell *158*, 25-40.

Jha, A.K., Huang, S.C., Sergushichev, A., Lampropoulou, V., Ivanova, Y., Loginicheva, E., Chmielewski, K., Stewart, K.M., Ashall, J., Everts, B., et al. (2015). Network integration of parallel metabolic and transcriptional data reveals metabolic modules that regulate macrophage polarization. Immunity *42*, 419-430.

Johnson, M.O., Wolf, M.M., Madden, M.Z., Andrejeva, G., Sugiura, A., Contreras, D.C., Maseda, D., Liberti, M.V., Paz, K., Kishton, R.J., Johnson, M.E., de Cubas, A.A., Wu, P., Li, G., Zhang, Y., Newcomb, D.C., Wells, A.D., Restifo, N.P., Rathmell, W.K., Locasale, J.W., Davila, M.L., Blazar, B.R., Rathmell, J.C. Distinct Regulation of Th17 and Th1 Cell Differentiation by Glutaminase-Dependent Metabolism. Cell. 2018 Dec 13;175(7):1780-1795.e19.
Kim, K.W., Williams, J.W., Wang, Y.T., Ivanov, S., Gilfillan, S., Colonna, M., Virgin, H.W., Gautier, E.L., and Randolph, G.J. (2016). MHC II+ resident peritoneal and pleural macrophages rely on IRF4 for development from circulating monocytes. J Exp Med *213*, 1951-1959.
Kojima, Y., Weissman, I.L., and Leeper, N.J. (2017). The Role of Efferocytosis in Atherosclerosis. Circulation *135*, 476-489.
Kuhn, R., Schwenk, F., Aguet, M., and Rajewsky, K. (1995). Inducible gene targeting in mice. Science *269*, 1427-1429.
Liu, P.S., Wang, H., Li, X., Chao, T., Teav, T., Christen, S., Di Conza, G., Cheng, W.C., Chou, C.H., Vavakova, M., et al. (2017). alpha-ketoglutarate orchestrates macrophage activation through metabolic and epigenetic reprogramming. Nat Immunol *18*, 985-994.
Marei, H., Malliri, A. GEFs: Dual Regulation of Rac1 Signaling. Small GTPases. 2017 Apr 3;8(2):90-99.
Morioka, S., Perry, J.S.A., Raymond, M.H., Medina, C.B., Zhu, Y., Zhao, L., Serbulea, V., Onengut-Gumuscu, S., Leitinger, N., Kucenas, S., et al. (2018). Efferocytosis induces a novel SLC program to promote glucose uptake and lactate release. Nature *563*, 714-718.
Nicklin, P., Bergman, P., Zhang, B., Triantafellow, E., Wang, H., Nyfeler, B., Yang, H., Hild, M., Kung, C., Wilson, C., et al. (2009). Bidirectional transport of amino acids regulates mTOR and autophagy. Cell *136*, 521-534.
O'Neill, L.A., and Artyomov, M.N. Itaconate: the poster child of metabolic reprogramming in macrophage function. Nat Rev Immunol. 2019 May;19(5):273-281
O'Neill, L.A., and Pearce, E.J. (2016). Immunometabolism governs dendritic cell and macrophage function. J Exp Med *213*, 15-23.
Papathanassiu, A.E., Ko, J.H., Imprialou, M., Bagnati, M., Srivastava, P.K., Vu, H.A., Cucchi, D., McAdoo, S.P., Ananieva, E.A., Mauro, C., Behmoaras, J. BCAT1 controls metabolic reprogramming in activated human macrophages and is associated with inflammatory diseases. Nat Commun. 2017 Jul 12;8:16040.
Stipanuk, M.H and Caudill, M.A. Biochemical, physiological and molecular aspects of human nutrition. 2013 International Book Number: 978-0-323-44181-0.
Tabas, I. (2010). Macrophage death and defective inflammation resolution in atherosclerosis. Nat Rev Immunol *10*, 36-46.
Tavakoli, S., Downs, K., Short, J.D., Nguyen, H.N., Lai, Y., Jerabek, P.A., Goins, B., Toczek, J., Sadeghi, M.M., Asmis, R. Characterization of Macrophage Polarization States Using Combined Measurement of 2-Deoxyglucose and Glutamine Accumulation: Implications for Imaging of Atherosclerosis. Arterioscler Thromb Vasc Biol. 2017 Oct;37(10):1840-1848.
Vats, D., Mukundan, L., Odegaard, J.I., Zhang, L., Smith, K.L., Morel, C.R., Wagner, R.A., Greaves, D.R., Murray, P.J., and Chawla, A. (2006). Oxidative metabolism and PGC-1beta attenuate macrophage-mediated inflammation. Cell Metab *4*, 13-24.
Viaud, M., Ivanov, S., Vujic, N., Duta-Mare, M., Aira, L.E., Barouillet, T., Garcia, E., Orange, F., Dugail, I., Hainault, I., Stehlik, C., Marchetti, S., Boyer, L., Guinamard, R., Foufelle, F., Bochem, A., Hovingh, K.G., Thorp, E.B., Gautier, E.L., Kratky, D., Dasilva-Jardine, P., Yvan-Charvet, L. Lysosomal Cholesterol Hydrolysis Couples Efferocytosis to Anti-Inflammatory Oxysterol Production. Circ Res. 2018 May 11;122(10):1369-1384.
Wang, Y., Subramanian, M., Yurdagul, A. Jr., Barbosa-Lorenzi, V.C., Cai, B., de Juan-Sanz, J., Ryan, T.A., Nomura, M., Maxfield, F.R., Tabas, I. Mitochondrial Fission Promotes the Continued Clearance of Apoptotic Cells by Macrophages. Cell. 2017 Oct 5;171(2):331-345.e22.
Yurdagul, A Jr., Subramanian, M., Wang, X., Crown, S.B., Ilkayeva, O.R., Darville, L., Kolluru, G.K., Rymond, C.C., Gerlach, B.D., Zheng, Z., et al. (2020). Macrophage Metabolism of

Apoptotic Cell-Derived Arginine Promotes Continual Efferocytosis and Resolution of Injury. Cell Metab *31*, 518-533.e10.
Yun, T.J., Lee, J.S., Shim, D., Choi, J.H., and Cheong, C. (2017). Isolation and Characterization of Aortic Dendritic Cells and Lymphocytes in Atherosclerosis. Methods Mol Biol *1559*, 419-437.
Yvan-Charvet, L., Pagler, T.A., Seimon, T.A., Thorp, E., Welch, C.L., Witztum, J.L., Tabas, I., and Tall, A.R. (2010). ABCA1 and ABCG1 protect against oxidative stress-induced macrophage apoptosis during efferocytosis. Circ Res *106*, 1861-1869.
Zhang, S., Weinberg, S., DeBerge, M., Gainullina, A., Schipma, M., Kinchen, J.M., Ben-Sahra, I., Gius, D.R., Yvan-Charvet, L., Chandel, N.S., et al. (2019). Efferocytosis Fuels Requirements of Fatty Acid Oxidation and the Electron Transport Chain to Polarize Macrophages for Tissue Repair. Cell Metab *29*, 443-456 e445.